

**Facies**

April 2021, Volume 67 Issue 2 Pages 17 (23p.)

<https://doi.org/10.1007/s10347-021-00624-1><https://archimer.ifremer.fr/doc/00684/79580/>**Archimer**<https://archimer.ifremer.fr>

---

## Sedimentology and distribution of late quaternary calciturbidites and calcidebrites in the Mozambique Channel (Southwest Indian Ocean)

Counts John W. <sup>1,2,3,\*</sup>, Jorry Stephan <sup>1</sup>, Vazquez-Riveiros Natalia <sup>1</sup>, Amy Lawrence A. <sup>2,3</sup>,  
Denniellou Ewen <sup>4</sup>, Jouet Gwenael <sup>1</sup>

<sup>1</sup> Unité Géosciences Marines, Institut Français de Recherche pour l'Exploitation de la Mer (IFREMER),  
Pointe du Diable, 29280, Plouzané, France

<sup>2</sup> School of Earth Sciences, University College Dublin, Belfield, Dublin 4, Ireland

<sup>3</sup> Irish Centre for Research in Applied Geosciences (iCRAG), O'Brien Centre for Science, University  
College Dublin, Belfield, Dublin 4, Ireland

<sup>4</sup> UniLaSalle, 19 Rue Pierre Waguet, BP30313, 60026, Beauvais, France

\* Corresponding author : John W. Counts, email address : [jwcounts@gmail.com](mailto:jwcounts@gmail.com) ;

[Stephan.Jorry@ifremer.fr](mailto:Stephan.Jorry@ifremer.fr) ; [Natalia.Vazquez.Riveiros@ifremer.fr](mailto:Natalia.Vazquez.Riveiros@ifremer.fr) ; [Lawrence.Amy@ucd.ie](mailto:Lawrence.Amy@ucd.ie) ;  
[Ewen.Denniellou@etu.unilasalle.fr](mailto:Ewen.Denniellou@etu.unilasalle.fr) ; [Gwenael.Jouet@ifremer.fr](mailto:Gwenael.Jouet@ifremer.fr)

---

### Abstract :

Submarine gravity flow processes on carbonate platform slopes can lead to the deposition of calciturbidite and calcidebrite beds on the adjacent deep-water seafloor. Such deposits have been previously found to occur more frequently during sea-level highstands, leading to increased export of carbonates to the deep sea during interglacial periods. Here, we document a new occurrence of these types of event beds in cores near a series of volcano-cored carbonate platforms in the Mozambique Channel (SW Indian Ocean), describing them from a sedimentological perspective and analyzing the controls on their distribution. 32 event beds, located near four isolated platforms, are composed primarily of uncoated skeletal grains from primarily shallow-water and planktic taxa. Compositional analysis shows that planktic foraminifera are hydrodynamically sorted such that they form a greater proportion of the upper parts of event beds. Age models based on foraminifer  $\delta^{18}\text{O}$  isotope data allow for precise (ky-scale) dating of each gravity flow event; results show that events occurred with frequencies ranging from 2 to 4 events per 100,000 years over the past ~800 kyr regardless of the phase within the sea-level cycle (i.e., transgressive, regressive, highstand or lowstand). However, events were most frequent during periods, both relative and absolute, of highest sea level, and are therefore interpreted to be controlled in part by sea-level status or change, though additional causes are also possible.

**Keywords :** Calciturbidite, Carbonate, Deepwater, Indian Ocean, Mozambique channel, Calcidebrite, Grainstone

## INTRODUCTION

Allochthonous deposits resulting from recent (Quaternary-present) submarine gravity flows are found on and around steepened carbonate margins at several locations around the globe (e.g., Crevello and Schlager, 1980; Jorry et al., 2008; Puga-Bernabéu et al., 2014). While numerous mechanisms responsible for triggering these flows have been proposed (reviewed in Reijmer et al., 2012), multiple studies (Haak and Schlager, 1989; Reijmer et al., 1992; Andresen et al., 2003; Jorry et al., 2008, 2010, 2020; Reijmer et al., 2012, 2015; Webster et al., 2012) have found a correlation between increased

abundance of these calcareous event beds and periods of eustatic highstand. However, more data from new and different regions and across differing time spans can help to test the universality of this 'highstand shedding' phenomenon, and may provide additional insight into the details of the processes and products associated with it. Analysis of such deposits on the modern seafloor may also assist in the interpretation of analogous sediments in the geologic record, where they are found at least as far back as the Ediacaran (Cochrane et al., 2019) and during all subsequent periods (e.g., Devonian-Carboniferous; Kalvoda et al., 1999; Triassic; Reijmer et al., 1994; Paleocene/Eocene; Robertson, 1976; Miocene; Sola et al., 2018). Additionally, carbonate gravity-flow deposits may be components of subsurface hydrocarbon systems (e.g., Winefield et al., 2011), and may therefore have economic importance. New case studies of these types of sediments therefore have implications beyond the region in which they are found.

To this end, this study documents a new occurrence of calciturbidites, calcidebrites, and hybrid event beds (often in the form of wackestones and packstones) from the deep seafloor of the Mozambique Channel (Fig. 1), and analyzes their sedimentologic character, the processes responsible for their deposition, and their stratigraphic distribution with respect to sea-level trends during the late Quaternary. Because the carbonate platforms from which these sediments originate are isolated and small in size, they offer an opportunity to examine these deposits from a source-to-sink perspective, providing insight into the various controls on their deposition and internal properties. This study is the first to describe and interpret these types of deposits in detail in the southwestern Indian Ocean, expanding their known range in modern systems and offering a new data set outside of better-known carbonate depositional systems in the Caribbean and elsewhere. The carbonate sand beds discussed herein are compared and contrasted with occurrences from other isolated carbonate platforms, placing them in a global context and relating them to previously developed carbonate facies models.

## **GEOLOGIC SETTING**

This paper focuses on sandy carbonate beds found in cores from the deepwater (2000-3500 m) seafloor near the Iles Eparses, a series of flat-topped, isolated, volcano-cored carbonate platforms in the Mozambique Channel, offshore east Africa. The four carbonate platforms discussed here (Glorieuses, Juan de Nova, Europa, and Bassas da India; Fig. 1) began as volcanic seamounts in the Cretaceous, and though the tectonic origins and underlying causes for the initiation of volcanic activity remain somewhat enigmatic, at least some of the volcanos in the Mozambique Channel are thought to be hotspot-related (Leroux et al., 2020). Although each of the four platforms have their own specific geological histories, they also share many similarities. Carbonate production, at least in Glorieuses and Bassas da India, began in the early Cenozoic (Paleocene-early Miocene, Courgeon et al., 2016). Subsequent aggradation has resulted in a several tens to hundreds of meters of carbonate buildup, and evidence exists in Bassas da India for continued volcanic activity until the Pliocene (Courgeon et al., 2017).

Platform tops are relatively flat, and their tops are tens of meters below sea level on average. Each platform is at least in-part subaerially exposed, usually resulting in small vegetated islands only a few kilometers across. The exception is Bassas da India, the only platform of the four with a continuous fringing reef, which is exposed only during low tide. The other three platforms (Glorieuses, Juan de Nova, and Europa) lack this defining characteristic, and are thus better considered carbonate banks. Jorry et al. (2016) reported sedimentological and geomorphological data from the Glorieuses, Juan de Nova, and Europa platform tops, finding subaerially exposed reefs from the last interglacial period (MIS 5) in conjunction with sedimentary deposits. Fragments of corals, green algae, molluscs and foraminifers make up the bulk of shallow-water sediment, with corals forming a lesser component in deeper water. The sedimentology of the shallow top of the Ile Glorieuse platform was also described in detail by Prat et al. (2016), who looked at the distribution of carbonate facies and found that sediments consisted primarily of a combination of skeletal elements from a variety of shallow-marine sources (e.g., corals, green and red algae, foraminifers) and only a minor fraction of mud. Counts et al. (2019) described sediment samples from the top of Juan de Nova, noting that these also consisted almost entirely of grains of carbonate sand-

sized and above. Based on the depositional pattern of aragonite mud in basin floor sediments, both Prat et al. (2016) and Counts et al. (2019) postulate that winnowing of fines during highstands results in a sand-dominated platforms in the present day, a phenomenon recognized in other carbonate environments as well (e.g., Paul et al., 2012; also see review in Counts et al., 2019) .

In addition to off-platform export of fines in suspension, the lack of a continuous topographic barrier (fringing reef) on most platforms permits the transfer of coarser sediments across the slope break. The platform slopes are relatively steep, with upper slope gradients around 25-35 degrees. Upper and middle slopes are characterized by outcropping volcanics and a thin sedimentary cover. Slope processes and products in all of the platforms discussed here were described in detail by Counts et al. (2018), who noted the presence of kilometer-scale upper-slope failure scars and associated mass-transport deposits (debrites) in seismic. These features suggest that at least some coarse-grained material, while initially sourced from the platform tops, may also originate from slope failure rather than direct input. Canyons and channels visible in bathymetry were interpreted as sediment transport pathways based on backscatter and core evidence (Counts et al., 2018). These channels terminate onto the lower slope and proximal basin floor, where they often form lobate bodies several kilometers across. Evidence for levee formation on channel flanks also exists, and plan-view backscatter imagery reveals short channel-lobe morphologies for some downslope sediment pathways. On the deep seafloor adjacent to platforms, Jorry et al. (2020) examined turbidites in two of the core discussed here, MOZ1-KS04 and MOZ1-KS07 (near the Glorieuses platform), finding that interglacial episodes corresponded with both a greater number of calciturbidite events, as well as a greater total thickness of turbidite deposits. Here, we examine some of these same sediments in greater detail, and incorporate new, unpublished core data from the other three studied platforms.

## **METHODOLOGY AND DATA SET**

The bathymetric and core data presented here were collected by Ifremer during a series of research cruises that took place in 2014 (PTOLEMEE, Jorry 2014; PAMELA-MOZ1, Olu 2014) and 2015 (PAMELA-MOZ4, Jouet and Deville 2015) aboard the R/Vs *Atalante* and *Pourquoi Pas?* as part of a larger campaign to better understand the geologic history of the Mozambique Channel and nearby areas (PAMELA research program; Bourillet et al., 2013). Piston coring (Kullenberg and Calypso) was able to recover several meters of seafloor sediment at numerous locations; the seven cores discussed here are between 4 and 27 meters long, and were selected for their proximity to carbonate platforms. Cores were collected from the lower slopes and proximal basin floor of each of the four platforms in question (Table 1) at distances of around 10-30 kilometers from their respective platform margins. Sampling was concentrated on the leeward side of the platforms, and most cores were located within a base-of-slope sediment wedge that is hypothesized to be linked to off-platform sedimentation.

Once collected, cores were split and logged onboard. Working halves, stored at the Ifremer CREAM core repository in Brest, France, were further described by the authors with respect to facies classification and identification of event beds. Grain-size analysis of selected intervals was performed for the sediment fraction between 10 nm and 2 mm (size fraction confirmed by sieving; analyzed sample size around 5 grams per sample) using a Malvern Mastersizer 3000 laser diffraction particle sizer. Other representative samples were selected for further analysis in thin section. Unconsolidated sandy sediments were washed and sieved to the 10 nm to 2 mm size fraction to aid in the identification of coarser allochemical grains. The washed sand fraction was then oven-dried and impregnated with resin before thin sections were produced. Thin sections were digitized with Nikon and Epson slide scanners in plane light at sufficient resolution (minimum 3200 ppi) to image the internal properties of individual sand-sized grains. Compositional analysis was then performed with a combination of a binocular petrographic microscope and thin-section scans using the point-counting software JMicrovision (Roduit, 2019) and a reference guidebook (Adams and MacKenzie, 1998). At least 300 grains at randomized points were counted per sample. X-Ray images shown in some figures were acquired with a X-CT Scanner manufactured by Geotek.

After core sediments were adequately characterized, time-depth relationships for each core (with the exception of MOZ1-KSF22 and MOZ1-KS27) were generated using the  $^{18}\text{O}/^{16}\text{O}$  ( $\delta^{18}\text{O}$  hereafter, expressed in ‰ vs. Vienna Pee-Dee Belemnite, VPDB) isotope record of benthic or planktonic foraminifera tests recovered from core sediments. Each core was sampled at 10- or 20-cm intervals, avoiding coarse-grained intervals when possible, and 2-8 well-preserved specimens of *Cibicidoides wuellerstorfi* were picked by hand, with the exception of core MOZ1-KS07 in which only the planktonic foraminifer *Globigerinoides ruber* was available. Selected individuals were homogenized and analyzed at the Leibniz Laboratory for Radiometric Dating and Stable Isotope Research at Kiel University, Germany, using a Kiel IV carbonate preparation device connected to a MAT 253 mass spectrometer from ThermoScientific. All laboratory internal and international standards (NBS-19 and IAEA-603) adhere to a precision of  $\pm 0.09\text{‰}$ . Before generating the age model, coarse-grained beds were removed from depth logs and depths were recalculated to produce a log that represented only the thickness of fine-grained sediments. This was done with the rationale that coarse-grained beds likely represent singular events that record a geologically instantaneous deposit, and these would adversely affect the best fit to the reference curve and calculation of sedimentation rates. The only exception to this procedure was core MOZ1-KS04, in which beds were retained so that the age model would be consistent with that reported in Jorry et al. (2020). Once event beds were removed, age models for each core were based on correlation of the benthic  $\delta^{18}\text{O}$  record to the LR04 benthic stack (Lisiecki & Raymo, 2005), using the program AnalySeries (Paillard et al., 1996). In the case of core MOZ1-KS07, lacking a benthic isotopic record, its *G. ruber*  $\delta^{18}\text{O}$  record was correlated to the planktonic  $\delta^{18}\text{O}$  of nearby reference record MOZ4-CS09 (Counts et al., 2019). Initial age models for cores MOZ1-KS04 and MOZ1-KS07 were first reported in Jorry et al. (2020), for core MOZ4-CS22 in Fierens et al. (2020) and for core MOZ4-CS09 in Counts et al. (2019). In these models, event beds were included, and they therefore differ slightly from those reported here, though the general age-depth relationships are very similar. Age model data, including tie points, are included as a table in the supplementary information. For most cores, the sawtooth pattern of  $\delta^{18}\text{O}$  values could be easily fit to the Lisiecki and Raymo (2005) LR04 reference curve, allowing core ages to be ascertained with confidence. Sea level values used in this

paper are from Spratt and Lisiecki (2016) unless otherwise noted, and Marine Isotope Stage values are from Cohen and Gibbard (2013). Although isotopes were extracted from core MOZ1-KS27, the shorter length of this core resulted in a non-diagnostic pattern of isotope changes, preventing correlation with the reference curve and the creation of a reliable age model. The short length of core MOZ1-KS22 also precluded isotopes from being analyzed for the same reason.

The proportion of various taxa was quantified by point-counting thin sections of several representative beds, although some significant component of each of the samples was unidentifiable, with around 30-40% of grains containing no diagnostic features. Despite this, enough constituent grains could be identified to characterize the general composition of the facies. Because some taxa may be more easily identifiable than others at certain size fractions, grains were categorized into classes based on the confidence level of their identification. Foraminifera, for instance, are easily identifiable at all size fractions and even when fragmented. *Halimeda* and other calcareous green algae are identifiable both in thin section and under the binocular microscope by their distinctive micritized texture and vesicular microstructure. This is often not the case for most other groups, who may break down into non-diagnostic grains of crystalline calcite or aragonite. Most of these other taxa (e.g., corals, bivalves, echinoids, etc.) were only identifiable in less than 3% of the total number of grains, often constituting only a few (<10) individual counts per sample. Due to this low abundance, an analysis of the changing taxonomic composition of a wide range of shallow-water taxa (c.f. Bernet et al., 2000; Reijmer et al., 2012) was not considered to be statistically meaningful. As such, the few identifiable shallow-water taxa were combined with more ambiguous grains to form three compositional categories: foraminifera, calcareous algae, and other/unidentified skeletal fragment. This classification not only avoids the pitfalls of inaccurate taxonomic identification, but is still reflective of the densities and hydrodynamic properties of grains; e.g., foraminifera generally behave as smaller particles due to their hollow chambers, whereas many skeletal fragments will likely behave similarly in a gravity flow regardless of their taxonomic affiliation. Twelve representative samples from cores MOZ1-KS04, MOZ1-KS07, MOZ4-CS23, MOZ4-CS09, and MOZ4-CS22 were chosen

from similar relative positions (slightly above the bed base) within several event beds and assessed for their composition with respect to these categories. Once analysis was complete, the events from which samples were sourced were classified as occurring during highstand, regressive, or transgressive intervals; too few events occurred during lowstand periods to be analyzed. Designation of these sea-level intervals was based on large-scale (glacial / interglacial) trends in sea level trajectory rather than small fluctuations (Table 2), using the reconstructed curve of Spratt and Lisiecki (2016).

The frequency of bed deposition was also calculated during each of these sea level phases (highstand, lowstand, transgression, or regression). 32 event beds in all were counted due to correlation of the 81-ka event between MOZ1-KS04 and MOZ1-KS07. Frequency of event bed deposition was assessed in terms of number of events per thousand years over the last 800 ky. This was due to the differing time spans of each sea-level phase: regression intervals during the Pleistocene, for instance, are generally longer and more gradual, whereas transgressive intervals are generally shorter and more rapid. Event frequency must therefore be normalized to account for these differences. Although each individual core does not fully cover this entire time frame, core coverage is not biased toward any given sea-level phase, and therefore the event frequency rates relative to one another are still meaningful. Three older beds in core MOZ4-CS23 were excluded from this analysis because: 1) they are significantly older than all other beds observed, and therefore required comparison with a different sea-level reconstruction (Miller et al., 2011); 2) the inclusion of long time spans not covered by most cores would lower the accuracy of depositional frequencies; and 3) sea-level changes during this older time frame were more rapid, which decreases the accuracy of the timing of bed deposition.

## **RESULTS**

In general, sediment cores are composed of unlithified clays and muds, interlayered with discrete beds of calcareous or clastic sands. These are classified into seven sedimentary facies, presented in Figure 2. Although there are occasional sharp changes in the color of the “background” muds, no

significant bounding surfaces are observed, and the overall architecture of each core is relatively similar throughout. Although cores were taken near multiple platforms across a large area, they are generally consistent in their overall composition, stratigraphic architecture, and sedimentation rates. Core locations, logs, stable isotope curves, age-models, and representative photos are shown in Figures 3 to 6. Coarse-grained clastic sediments (Facies 6 and 7) and fine-grained muds (Facies 1), while included in the facies classification scheme, are outside the focus of this study and are not discussed in detail; this study focuses on carbonate Facies 2 through 5.

## **Sedimentary Facies and Stratigraphic Architecture of Carbonate Gravity Flow Deposits**

### *Facies Classification*

Sediments found in cores can be classified into seven distinct facies (Fig. 2), broadly comprising the categories of “background” muds (Facies 1 and 2), carbonate beds with a substantial component of sand-sized grains (Facies 3, 4, and 5), and clastic and glauconitic sands (Facies 6 and 7). Facies 1 consists of laminated or bioturbated hemipelagic or aragonitic muds and is seen in all cores (Figs. 3-6). Aragonite and clay content may vary cyclically in response to sea-level change; Counts et al. (2019) provide a detailed analysis of the sedimentological character and controls on these types of sediments in the areas surrounding platforms. These sediments also contain a sizable portion (typically ~20-40% by volume, though greater values may occur) of the hollow tests of semi-spherical planktonic foraminifera, increasing the volume percentage of sand-sized particles recorded in grain-size analysis. Facies 2 is composed of the same general lithology, but is texturally different. Rather than laminations or diffuse burrow mottling, this facies is chaotically bedded and contains discrete cm-scale clasts of muds with a slightly different color, related to slight differences in lithology (Fig. 3D). Facies 3-5 are characterized by a significant increase in the amount of carbonate sand (defined as particles composed of  $\text{CaCO}_3$  with a diameter of  $63\mu\text{m}$ -2mm) relative to finer-grained Facies 1 and 2. These facies are found in discrete beds and are distinguished by the amount and nature of co-depositional mud and/or clay. Facies 3 and 4 contain variable amounts of interstitial mud and clay, forming wackestones (mud-supported carbonate rock that contains greater than

10% grains; Facies 4) or packstones (grain-supported carbonate sediments that contain 1% or more mud-grade fraction; Facies 3 and 5) (Dunham, 1962). Sedimentary structures are rare or absent, though planar- and cross-lamination may both occur. Facies 5 is also composed primarily of packstones, but additionally contains centimeter-scale clasts of Facies 1 muds. Remaining facies (6 and 7) are dominated by micaceous quartz and glauconite sands, respectively, and are generally only a few centimeters in thickness. These may be laminated at the bases of beds, and also often fine upwards. Each of these facies are typically contained within discrete beds, in most of the cored sediments.

### *Texture and Internal Architecture of Carbonate Sand Facies*

Carbonate sand beds of Facies 3, 4 and 5 have varying amounts of mud (Figure 7, supplementary data). Grain size trends within individual beds are variable (discussed below), but most often massive or fining-upward; changes in mud content within a bed may result in a gradual upward change from Facies 5 to Facies 4 to Facies 1. Occasional examples of amalgamated beds occur, including MOZ1-KS07 (655-675 cm), however, these beds are relatively similar in character, differing only in their specific grain size profiles. Thicknesses of beds containing these facies range from <1 cm to over 1 m thick, with the modal bed thicknesses being at a cm-scale, but with many beds reaching several tens of centimeters; these often display sharp bases and sharp or gradational tops. Grain shapes are almost always angular or sub-angular. The basal parts of many of the thicker beds contain a lag deposit of skeletal fragments up to pebble size, composed primarily of coralgall and bivalve material. The median grain size (D50) of sediments in ranges from <100 to >600  $\mu\text{m}$ , and mud proportion ranges from 6 to >75% by volume (see supplementary data). Grain size analysis within individual beds (Fig. 7) reveals several styles of vertical distribution of sand-sized particles that generally correspond to certain facies: disorganized (Facies 5; Fig. 7A), weakly graded (Facies 3, grading upward into Facies 4; Fig. 7B, 7D, and 7E), and generally massive (though with a very slight fining-upward trend; Facies 5; Fig. 7C). Similarly, mud content may be unevenly distributed (Fig. 7A), generally consistent (Figs. 7C, 7D), or with maxima near the top and bottom of the bed and lowest mud content in the middle (Figs. 7B, 7E). Median grain sizes in most of these beds are

most often in the fine- and medium-grained sand range (0.125-0.5 mm). Where observed, sedimentary structures in these facies generally consist of planar laminae, as seen clearly for example in the radiograph image of core MOZ4-CS09 (Fig. 3C). The only bed with multiple sedimentary structures is in interval 1393-1443 cm of core MOZ4-CS22 (Fig. 6C), where a clear vertical succession from massive (Bouma  $T_a$  division), to planar-laminated ( $T_b$ ), to ripple-laminated ( $T_c$ ) carbonate sands is evident across the 50 cm thickness of the bed, forming a partial Bouma sequence (Bouma, 1962).

Facies 5, while also being packstone-dominated, also contains large rip-up clasts of background muds entrained within the bed. It is found only in two cores, including the lower part of core MOZ4-CS23 (Fig. 5B-5C), and the thickest (over 1 meter) carbonate sand bed observed in the study, core MOZ1-KS27 (157-256 cm, Fig. 6D). In the latter, these mud clasts coarsen upwards, reaching decimeter-scale. This bed is sandwiched between two thinner, fining-upward beds composed of cleaner carbonate sands. Although these beds are in stratigraphic continuity, they can be distinguished from one another by a relatively sharp surface and a change in lithological character.

### *Composition of Carbonate Sand Facies*

Sand-sized grains in Facies 3, 4 and 5 are almost entirely composed of the skeletal fragments of calcareous organisms, including bivalves, echinoids, corals, and red and green algae (Fig. 8A, 8B). Planktonic taxa are also present, including foraminifera and rare pteropods. In almost all samples, dominant grains were either fragments of the calcareous green algae *Halimeda*, or chambered or spherical planktonic forams. The relative proportion of taxonomic categories within individual carbonate sand deposits varies vertically within beds, as illustrated in core MOZ1-KS04, Figure 8C, interval 611-641. Composition also differs between the different size fractions of the same sample, as shown in Figure 8D, core MOZ4-CS09, interval 338-340; first reported in Counts et al. (2018). In this case, the proportion of (dominantly planktonic) foraminifera is higher within finer-grained samples, indicating that the increased abundance of foraminifera upwards within a bed (illustrated in Fig. 8C) is likely related to normal grading.

Some thin beds (e.g., interval 2548-2550 in core MOZ4-CS23; Fig. 8E) are composed almost entirely of a layer of planktonic foram tests.

Samples examined for composition with regard to sea level trend (Fig. 8E; trend definitions discussed above) were generally taken from the just above the bases of beds with a range of thicknesses. Samples from beds deposited during Marine Isotope Stages 5, 7, and 9, regarded as “highstand” intervals, showed a higher overall proportion of foraminifera compared to those in during times of forced regression (~35-55% of constituents in highstand intervals, vs. 8-25% during regressions). Although the sample size is small, an ANOVA test of highstand-transgression-regression foraminiferal abundance indicates that statistically the difference is significant ( $\alpha=0.05$ ;  $p\text{-value}=0.02$ ; see supplementary data). The two samples analyzed during transgressive intervals show a wide range of variability in foram abundance, from almost 90% of grains, to less than 25%, though the former is thought to be from a differing depositional process. Samples taken within a bed where the age of deposition (and thus sea level) is unknown (MOZ1-KS27; samples on the right-hand side in Figure 8E) showed a distribution intermediate between the two; this bed was analyzed due to its inferred different depositional process from most other beds (discussed below). For comparison, the abundance of planktonic foraminifera was cross-plotted against several other variables (see supplementary data): absolute sea level height (relative to present), bed thickness, and position within the bed (expressed as a percentage from bottom of total bed thickness; values are averaged and approximate due to sampling thickness). Except for a broad relationship with sea level, none of these yielded especially significant correlations ( $R^2$  values of 0.23, 0.27, and 0.20, respectively), and thus were not interpreted to exert a strong degree of control over bed composition. Beds in core MOZ1-KS27 were excluded from these analyses due to its lack of an age model.

### *Event Bed Distribution*

Although beds initially seem to be randomly distributed throughout each core, analysis of bed frequency with respect to sea-level trends at the time of deposition reveals that bed deposition may have a

weak relationship with sea level (Fig. 9). Beds younger than 800 ka were most frequently deposited during highstand intervals (Fig. 9D, 0.047 events per ky), followed by regression as the second most common depositional phase (0.035 events per ky), lowstand (0.031 events per ky), and transgression (0.027 events per ky) and. The frequency of bed deposition was also calculated for absolute sea level values relative to present (Fig. 9E). This shows that event frequency was proportionally highest during periods of higher sea level compared to the present-day. Although this appears to confirm the increased frequency during highstand phases discussed above, only two events were recorded during these short high sea-level intervals, and thus these results should be treated as tentative. Event frequencies at other sea-levels varied, but show no clear trends toward increased deposition at highstands or lowstands.

### *Process interpretation*

Individual beds composed of packstones (Facies 3) and wackestones (4) are present in all the cores and display a variety of features that suggest that their origin is related to deposition by submarine gravity flows. Specifically, most beds of Facies 3 and 4 are interpreted to be turbidite deposits, as the grain size distribution and sedimentary structures (where present) within these deposits are consistent with partial Bouma sequences. Not all intervals with an increase in grain size were considered event beds; in some cases where sands were very thin or discontinuous, the origin of the bed was not clear. Variations in mud content are interpreted to be a product of variability in the source material, though the general lack of mud on platform tops indicates that mud in these beds was likely entrained in the flow at a later stage.

Calcareous sand beds containing large mud clasts (Facies 2C) are interpreted to represent debris flow deposits, as evidenced by the presence of coarsening-upward mudclasts and the unstructured, poorly sorted nature of the sandy and muddy matrix. When this type of deposit is in contact or close stratigraphic proximity with fining-upward turbidites, the combined package is interpreted to represent a hybrid event bed (*sensu* Haughton et al., 2009), whereby a single flow event may generate an event bed composed of deposits from multiple flow types. This is interpreted to be the case in core MOZ1-KS27, where multiple facies are present in close stratigraphic continuity.

The composition of calcareous taxa within these beds, including many taxa restricted to the photic zone, indicates that such events were ultimately sourced from the platforms themselves. This composition, however, does not preclude a multi-stage depositional process with an initial platform source. Initial deposition and winnowing may initially take place on the shallow platform; transfer across the platform margin may result in a second phase of deposition on the upper or mid-slope, where sediments may then move further downslope and onto the basin floor due to slope failure. Counts et al. (2018) and Jorry et al. (2020) noted the existence of active downslope sediment pathways within shallow canyons and channels on the Iles Eparses platform flanks, which are the likely source of the turbidites, debrites, and hybrid event deposits seen in cores.

### *Spatial extent of event beds*

Unfortunately, little direct information exists regarding the extent of turbidite beds. Most event beds are buried below the imaging capability of reflectivity/backscatter data due to their limited thickness and depth (more than 2 m below the surface). Additionally, at only a few tens of centimeters thick, event beds are well below the resolution of even the highest-quality seismic data acquired in the basin. Jorry et al. (2020), however, note that seafloor ridges (possible sediment waves or erosive troughs related to cyclic steps) and low-amplitude seismic reflection packages interpreted as debrites near the Glorieuses platform may reveal the extent of the seafloor affected by gravity flows, estimating that these features may be present at more than 40 km from the platform margin.

Direct information regarding the extent of turbidites are therefore best obtained from cores themselves. Of the core described in this study, MOZ1-KS07 is located the farthest from its platform margin at a distance of 34 km. Although the carbonate event beds discussed here may originate from parts of the slope below the margin, this distance is the maximum observed run-out length of a turbidite event in the Iles Eparses (though total length may be greater than observations). Deposition of calciturbidites likely continues further into the basin, but the relative paucity and limited thickness of carbonate beds in this core

suggests that this distance is approaching the distal limit of deposition. Although large-scale slope failure events elsewhere may generate turbidity currents that travel for hundreds of kilometres (e.g., the Grand Banks event; Piper et al., 1988; the unconfined Storegga Slide; Hafliðason et al., 2005), the failures seen in the Iles Eparses are generally much smaller in volume,  $<10 \text{ km}^3$  (Counts et al., 2018), and run-out lengths on the order of tens of kilometres are reasonable (e.g., Talling et al., 2013). Coring locations were not selected with the goal of correlating individual events, but rather for obtaining a representative view of off-platform deposits. Only one event is tentatively correlated between cores MOZ1-KS04 and MOZ1-KS07, based on the timing of deposition at ~81-82 ka (Fig. 4B). These cores are approximately 17 km apart, and if correct, is consistent with turbidite extents of 10's of km on the basin floor. The mud content in this bed increases substantially basinward, from around 8% in MOZ1-KS04 to around 75% in MOZ1-KS07.

## **DISCUSSION**

### **Distribution of gravity flow events**

Unlike the base-of slope wedges of clastic sediments deposited during lowstands, carbonate transfer into the deep sea has long been known to increase in volume during times of high sea level (Schlager et al., 1994). Causes for this difference are generally attributed to the increased carbonate production and export when platform tops are flooded (e.g., Chabaud et al., 2016), though the geomorphology of the margin and slope also plays a role in turbidite distribution (Puga-Bernabéu et al., 2014). This transfer may take the form of fine-grained aragonite that is transported in suspension and redeposited as a component of seafloor muds (e.g., Droxler et al., 1990; Schlager et al., 1994; Lantzch et al., 2007; Paul et al., 2012; Betzler et al., 2013), or as the more discrete, episodic transfer of carbonate sands to the deep sea by sediment gravity flows (e.g., Droxler and Schlager, 1985; Haak and Schlager, 1989; Andresen et al., 2003; Jorry et al., 2008). The former mechanism has previously been proposed for the Juan de Nova platform (Counts et al., 2019). The data presented in this study also show that transport by sediment gravity flows is also an important downslope transport mechanism for sediment from

carbonate platforms of the Mozambique Channel, expanding the findings of Jorry et al. (2020). The results shown here indicate that turbidite events over the time period considered are more frequent (by a rate ~35-50% greater than other sea level intervals, as defined here) during the highest sea level intervals and during relative highstand periods (Fig. 9).

The data in Figure 9, however, shows that numerous events occur during times of transgression, regression, and lowstand as well. This temporal distribution indicates that gravity flow initiation is triggered during all phases of sea level, and must therefore either: 1) have multiple sea-level-related causes, each of which operates with a different frequency during different phases, or 2) have an alternative cause independent of sea level, but is also overprinted by sea-level-induced triggering that increases the number of gravity flow events during relative highstands. Although neither of these scenarios can be explicitly ruled out with the present data set, the latter is inferred to be the most likely here. The exact triggering mechanism of carbonate margin turbidity currents elsewhere has been hypothesized to be related to wave-base changes, overpressure due to various causes, pore drainage (none of which operate exclusively during highstand; see Spence and Tucker, 1997 and review in Reijmer et al., 2012), and/or oversteepening of margins due to increased platform top sedimentation during highstand (Reijmer et al., 2015). Gravity flow initiation on carbonate margins has also been attributed to seismic or tectonic activity (with respect to calcidebrites; Payros and Pujalte, 2008) and other independent causes (e.g., differential compaction; see review in Drzeweicki and Simó, 2002). Here, a combination of platform margin oversteepening, increased highstand carbonate production, and seismic activity as causal mechanisms would explain the observed distribution pattern (i.e., the presence of failure events during all sea level phases and in the complete range of absolute values, combined with increased frequency of events during highstand). This is circumstantially supported by the fact that: 1) the margins of Iles Eparses platforms are steep, generally around 25-35 degrees, in the upper range of ancient and modern carbonate slope angles described by Kenter (1990) and locally higher; compared to 4-12 degrees (though locally higher) in the Bahamas, and are therefore closer to the failure threshold and more prone to oversteepening-related failure, 2) the

Mozambique Channel is a tectonically active region with numerous earthquakes occurring in the present day (Deville et al., 2018; ISC, 2019), and 3) no evidence of pockmarks, gas escape, or other signs of overpressure are seen on the platform slopes (Courgeon et al., 2016, 2017; Counts et al., 2018). Slope failures scars are visible on all platform flanks, and are likely to be the source of at least some gravity flow events, though the mechanism by which they are initiated is unknown (Counts et al., 2018). Although Andresen et al., (2003) noted that sea level is the primary driver of turbidite deposition even near the tectonically active Pedro Bank in the Caribbean, the genetic and geomorphological differences with the Iles Eparses may result in higher susceptibilities to seismic activity. Indeed, earthquake-induced failure and turbidity current generation on carbonate margins has previously been interpreted from ancient settings (e.g., Johns et al., 1981). Additionally, there is no *strong* correlation here between sea-level phase (highstand, lowstand, transgression or regression), sediment composition (except for foram abundance), and/or depositional process (turbidites vs. debrites) as seen in the Bahamas by Reijmer et al. (2012) and used to infer a purely sea-level driven cause of flow events. The morphology of the platform slope and margin may also play a role in event bed distribution, as found in the mixed carbonate-clastic system of the Great Barrier Reef (Australia; Puga-Bernabéu et al., 2013, 2014). There, calciturbidites were found to be more common in areas without physiographic barriers or canyons that allowed siliciclastics to bypass fringing reefs and enter the basin. Though not all of those findings are applicable to the small, isolated platforms discussed here, they highlight the potential importance of morphological controls on highstand shedding—future studies in the Iles Eparses and elsewhere may do well to systematically examine this issue. Other potential causes for event triggering that cannot be ruled out include climate (e.g., periods of increased aridity/humidity and changes in monsoon frequency), oceanographic processes such as internal waves and eddies (Miramontes et al., 2020) and volcanic activity, though these have not traditionally been tied to calciturbidite deposition.

## **Controls on Sedimentology**

Turbidites in the Iles Eparses are composed almost entirely of skeletal fragments, unlike most other calciturbidite examples in the world that often contain complete or partial ooids, grapestones, aggregates or lithic fragments, peloids, and various other types of carbonate grains (Haak and Schlager, 1989; Andresen et al., 2003; Reijmer et al., 1992, 2012, 2015). This compositional homogeneity is likely related to the initial composition of platform top sediment. Prat et al. (2016) found that platform top sediments on Ile Glorieuses are almost universally composed of skeletal fragments of algae, coral, molluscs, foraminifera, and other taxa. Such a composition is typical for Pacific and Indian Ocean carbonate platforms; unlike those in the Atlantic and Caribbean, the production of non-skeletal grains is much rarer here, a fact attributed by some (Milliman, 1974) to the generally deeper platform depths. Additionally, the geochemical conditions in the Atlantic and Caribbean (pH, aragonite saturation state) are more favorable to aragonite precipitation than those elsewhere (Lee et al., 2006; Gledhill et al., 2008, Prat et al., 2016). Deepwater calciturbidites originating from the Great Barrier Reef (Pacific Ocean, NE Australia) are also composed almost entirely of skeletal fragments, supporting this trend (Puga-Bernabéu et al., 2014). The difference in composition with regard to skeletal versus non-skeletal components seen in highstand and lowstand gravity flow deposits seen elsewhere (e.g., Reijmer et al., 2012), is therefore not replicated in the Iles Eparses. Even if sediment were alternately sourced from the platform margin and platform interior during glacial and interglacial periods, respectively, as proposed by Reijmer et al. (2012, 2015), the lack of grain diversity in the Iles Eparses would likely not allow for differentiation of these source areas.

The abundance of pelagic material in highstand deposits is also in contrast to the findings of Reijmer et al. (2012, 2015), who found increased foraminiferal content in lowstand event deposits. The difference in the (largely planktonic) foraminiferal content between highstands and lowstands cannot simply be attributed to an increase in foraminifera-bearing mud within the bed, as no correlation exists between mud content of samples and foram abundance (Fig. 8E). Instead, it may be due to increased highstand productivity of forams during warmer interglacials, as has been documented elsewhere (e.g., Xu et al., 2005). Planktonic foraminifera incorporated into turbidites may be a part of the initial grain assemblage on

the platform top, or may be incorporated into the sand-sized component of the bed through erosion of foram-rich seafloor mud along the course of the turbidite path. During highly productive times, the uppermost layer of foraminiferal ooze on the seafloor may be especially enriched in planktonic forams, allowing them to be easily incorporated into the flow deposit. This erosion may indicate a phase of slope bypass and the possible detachment of the flow deposit from the bathymetrically higher parts of the platform.

Examples of debrites are recorded in cores MOZ1-KSF22 and MOZ4-CS23. These have very different sedimentological character from one another, likely reflecting their individual provenance. The example in core MOZ1-KSF22, composed only of muds and lacking a sand-dominated component, may have been the result of a slope failure unrelated to an active channel or canyon system where coarse-grained sediments dominate. The debrite in cores MOZ4-CS23 is dominated by carbonate sands, and was deposited by an erosive flow as evidenced by the large clasts of laminated background mud incorporated into the sandy matrix. Although large-scale slope failure scars (failed sediment volumes on the order of less than ten km<sup>3</sup>) seen on platform flanks (Counts et al., 2018) may have resulted from seismic or volcanic events, these are interpreted to generate the much thicker mass transport deposits seen in the subsurface in seismic lines, rather than the meter and cm-scale deposits described here, which are below the resolution of seismic data.

In core MOZ1-KS27, the sequence of beds sedimentary structures, and sorting trends are very similar to the idealized hybrid event bed illustrated by Haughton (2009), where flows “transition or switch from non-cohesive to cohesive behaviour during deposition, followed by a variably developed, but generally volumetrically minor dilute turbulent wake”. Though such deposits are typically associated with siliciclastic deposits, they should not be unexpected in this carbonate setting as well. The predominance of turbidites in cores rather than debrites may be a function of the distance from the base of slope. This would allow flows additional time and distance to become turbulent compared those that are more proximal, and would imply that debris flows had runout distances shorter than those of turbidity currents. However, sediment

gravity flows may not always follow this path of increasing downslope flow dilution, as the presence of hybrid event beds can attest.

## **Depositional model**

Cored sediments provide the basis for a generic model for calciturbidite deposition in the basin (Fig. 10) that is consistent with simple hydrodynamic principles in which the downslope sedimentology of the bed mirrors that of an earlier vertical sedimentological succession (e.g., Bouma, 1962; Lowe, 1982, and others, summarized in Shanmugam, 2016). The slope failures that generate turbidites likely began as translational slides or slumps on the steep platform flanks. These sediments are composed primarily of sands sourced from the platform top, but with an increasing component of hemipelagic mud away from the platform. The studied cores, located >10 km from platform margin, do not preserve these submarine landslide deposits, indicating that either slope failure has limited runout distances or underwent relatively rapid transformation into debris flows and turbidity currents. Muddy debrites seen in cores (e.g. MOZ1-KSF22) likely represent the flows that are sourced from flank sites without a substantial component of platform-sourced sediment, perhaps lower on the slope. Most proximal deposits of sediment gravity flows on the basin floor or lowermost slope (e.g., Mulder and Alexander, 2001) (Fig. 10A). Some gravity flows may have undergone transformation to form hybrid flows as suggested by beds with both debritic and fining-upward sandy turbidite intervals (core MOZ1-KS27; Fig. 10B) (Haughton et al., 2003, Haughton et al., 2009). Moving downstream, a progressive increase in sediment support by turbulence leads to loss of debris flow component and deposition of mixed skeletal grain and foraminifera turbidites (similar to a Bouma *Ta* division; Fig. 10C). Alternatively, turbidite beds may be initiated as turbidites and remain so; a hybrid event bed precursor is not required for subsequent parts of the model. The progressive deposition of relatively coarse-grained material increases the proportion of fines (including mud) transported by the flow, resulting in a reduction in the median grain size both distally and vertically upwards within a bed, and at times an upward increase in mud content. These intervals, however, may only show a slight normal grading due to the lack of fines in the initial transported sediment, as well as the bypass of the suspended

load to more distal locations. Beds also become progressively partitioned distally in terms of composition, as planktonic foraminifera behave as hydrodynamically smaller particles and are sorted to the top of the bed (Fig. 10D). Experimental data (Hodson and Alexander, 2010) have shown that planktonic foraminifera have a generally lower settling velocity than other types of carbonate grains. Eventually, foraminifera may become the dominant component of beds (Fig. 10E) before they thin out and deposit any remaining sediment in the flow (Fig. 10F). Reworking by contour currents may occur at any of these stages, as deepwater currents are known to operate on the basin floor (Miramontes et al., 2019; Thieblemont et al., 2020). The lowest mud content is often found within the middle of event beds (Fig. 7). This is possibly due to 1) poorer sorting at bed bases related to an initial phase of rapid sedimentation due to loss of capacity, and 2) suspended load fallout and increased mud deposition near bed tops during final waning flow phase.

### **Analogues and Implications**

The model and observations presented here are similar to classic facies models for turbidites that relate depositional characteristics to phases of the turbidity flow, and fit into larger-scale (in both a temporal and spatial sense) carbonate slope depositional models developed by Playton et al. (2010) and others, including Reijmer et al. (2015), who developed facies models relating the composition of Cretaceous off-platform deposits to the proximal-distal evolution calcidebrites to calciturbidites. However, facies models incorporating grain texture and composition at a bed-scale have not previously been developed at this level of detail for modern carbonate gravity flows. While some aspects of the model presented in Figure 10 are specific to the deposits observed near the Iles Eparses, it is reasonable to assume that similar patterns (e.g., the hydrodynamic segregation of spherical and chambered planktonic foraminifera) may also happen elsewhere, as these grain types have a global distribution and a long geologic history. Foraminiferal grainstones as a component of calciturbidites have been described from the Eocene of Egypt (Corlett et al., 2018), and calciturbidites with up to 92% planktonic components have been described from the Miocene of Australia (Betzler et al., 1995). Bornhold and Pilkey (1971) report the lateral segregation of skeletal components in Bahamian calciturbidites in much the same way as that seen here, wherein

planktonic foraminifera content increases distally as *Halimeda* elements are no longer able to be transported. Andresen et al. (2003) also reported an increase in pelagic grains in calciturbidite beds at more distal locations, for the same reasons noted here. Observations from the Iles Eparses therefore add additional evidence to the universality of such processes across the globe and the geologic time scale.

The facies model shown here also has implications for analogous beds in, for example, subsurface petroleum systems, where the downslope and in-bed changes in mud content, as well as the compositional sorting of planktonic foraminifera, likely affect the deposit's porosity and permeability. Calciturbidites are known to form hydrocarbon reservoirs (Winefield et al., 2011), and are found throughout the geologic record (e.g., the Paleogene of Spain; Everts, 1991, the Devonian-Carboniferous of the Czech republic; Kalvoda et al., 1999; the Triassic of Europe; Maurer et al., 2003 & Sudiro, 1996, the Cretaceous of Albania; Rubert et al., 2012, the Cretaceous of France; Reijmer et al., 2015, the upper Tortonian of Spain; Sola et al., 2017, 2018, among others). Iles Eparses upper slope canyons/channels and lower slope channel-fan deposits (figured in Counts et al., 2018 and Jorry et al., 2020) are similar to the “basinal, grain-dominated channel-fan systems” in the facies model proposed by Playton et al. (2010) and to “calciclastic submarine fans” (CSFs) described by Payros and Pujalte (2008). These examples, however, are generally from linear continental margins rather than kilometre-scale isolated platforms like those seen here. Little is known about the allochthonous carbonate deposits flanking atolls and atoll-like platforms, as such deposits are relatively rare in the geologic record (see examples, however, in Mazzullo and Mazzullo, 1983, Da Silva et al., 2009, Peyrotty et al., 2020), and there is little basis for comparison as the specific settings of these fossil atolls are quite different than that seen here. Iles Eparses data thus provides a unique insight into the sedimentary character of an understudied carbonate depositional setting.

## **SUMMARY AND CONCLUSIONS**

This study presents the first sedimentological analysis of deepwater carbonate gravity-flow deposits in the Mozambique Channel, and is one of only a few studies to examine these types of deposits in modern

systems outside of the Caribbean. Core from the deep seafloor near a series of carbonate-topped platforms in the Mozambique Channel reveal numerous calciturbidites and calcidebrites resulting from gravity flow events that originated from the flanks or tops of platforms. Events were generally more common during periods of highstand and regression, as well as during periods of relatively high sea level. This agrees with observations of turbidite highstand shedding seen elsewhere, though the presence of event beds in all sea-level phases indicates that other factors are also at work. Indeed, this study confirms the results of several recent studies that show that the export of carbonates to the deep sea is more complex than a simple highstand shedding model suggests. Carbonate grains within beds are primarily composed of skeletal elements derived from the platform tops, and highstand-lowstand differentiation in the abundance of pelagic components. The hydrodynamic segregation of planktonic foraminifera is incorporated into a depositional model for the gravity flow deposits seen here, which is consistent with observations made by others in calciturbidites elsewhere. Results and interpretations presented in this study contribute to better characterization of the controls, character, and distribution of carbonate sediments exported to the deep sea, which are well-represented in the geologic record.

## **DATA AVAILABILITY**

Sediment cores collected in the Glorieuses basin are curated at IFREMER core repository in Plouzané (France). Core data related to this article can be requested at:

Core PAMELA-MOZ1-KS04: IGSN BFBGX-127668 (<http://igsn.org/BFBGX-127668>)

Core PAMELA-MOZ1-KS07: IGSN BFBGX-127671 (<http://igsn.org/BFBGX-127671>)

Core PAMELA-MOZ1-KSF22: IGSN BFBGX-127678 (<http://igsn.org/BFBGX-127678>)

Core PAMELA-MOZ1-KS27: IGSN BFBGX-127683 (<http://igsn.org/BFBGX-127683>)

Core PAMELA-MOZ4-CS09: IGSN BFBGX-85852 (<http://igsn.org/BFBGX-85852>)

Core PAMELA-MOZ4-CS22: IGSN BFBGX-128007 (<http://igsn.org/BFBGX-128007>)

Core PAMELA-MOZ4-CS23: IGSN BFBGX-128008 (<http://igsn.org/BFBGX-128008>)

## ACKNOWLEDGEMENTS

PAMELA-MOZ1 and PAMELA-MOZ4 cruises were co-funded by TOTAL and IFREMER as part of the PAMELA (Passive Margin Exploration Laboratories) project, in collaboration with IFPEN, Université de Rennes, Université de Brest, UPMC, and CNRS. This work was supported by the “Laboratoire d’Excellence” LabexMER (ANR-10-LABX-19) and cofounded by a grant from the French Government under the program “Investissements d’Avenir,” and by a grant from the Regional Council of Brittany (SAD program). Support during manuscript drafting also came from the Irish Centre for Research in Applied Geosciences (iCRAG) and the Department of Earth Science at University College Dublin. We thank the Captain and the crew of the R/Vs *L’Atalante* and *Pourquoi pas?*, as well as the scientific participants in the PAMELA-MOZ1 and PAMELA-MOZ4 surveys. Thanks also to Nils Andersen at Kiel University for isotope work and Greg Van den Bleeken at University College Dublin for laboratory assistance. Additionally, thanks are due to Dr. Ángel Puga Bernabéu, an anonymous reviewer, and journal editor Maurice Tucker for thorough and helpful comments on this manuscript, which improved it greatly.

## FIGURES

Figure 1: Shaded bathymetric map of Mozambique Channel (Envisat advanced synthetic aperture radar (ASAR) imagery) and satellite imagery of adjoining land areas. Circled areas are platforms discussed in this study; these constitute a part of the “Iles Eparses”, a group of French territories in the Indian Ocean. White areas onshore are cloud cover. Maps of individual core locations included in Figs. 3-6.

Figure 2: A) Classification of facies seen in cores. Color of box corresponds to bar on left side of core photos and diagrams in Figures 3-6. B) Lithologic patterns used in core logs in Figures 3-6. C) Water depth color shading used in core locator maps in Figures 3-6.

Figure 3: Cores from the area surrounding the Juan de Nova platform. A) Map showing locations of cores MOZ4-CS09 and MOZ1-KSF-22. B) Lithologic log,  $\delta^{18}\text{O}$  isotope record, and event bed ages for core MOZ4-CS09. LR04 benthic stack (Lisiecki and Raymo, 2005) for comparison. MIS = Marine Isotope Stage. C) Photograph and X-Radiograph of calciturbidite bed found between meters 3 and 4 in core. Color bar = facies; vertical tick marks in cm. D) Lithologic log of core MOZ1-KSF22, as well as photograph and X-Radiograph of portion of mud-dominated mass transport deposit seen between meters 2 and 4 (from core top) in left-hand core log.

Figure 4: Core from the area surrounding the Glorieuses platform. A) Map showing locations of cores MOZ1-KS04 and MOZ1-KS07. B)  $\delta^{18}\text{O}$  isotope record, lithologic logs, and event bed ages for cores MOZ1-KS04 and MOZ1-KS07. LR04 stack (Lisiecki and Raymo, 2005) shown in blue to far left based on global benthic foraminifera data. MIS = Marine Isotope Stage. C) Representative lithologies and facies (color bar) seen in cores MOZ1-KS04 and MOZ1-KS07. Core names and depths labeled; vertical tick marks in cm.

Figure 5: Core from the area surrounding Ile Europa. A) Map showing locations of core MOZ4-CS23. B) Lithologic log, facies, event ages, and  $\delta^{18}\text{O}$  profile for core MOZ4-CS23, and LR04 benthic stack (Lisiecki and Raymo, 2005). C) A selection of representative calciturbidite beds from core MOZ4-CS23, including those of muddy Facies 2B (green color on left bar) and 'cleaner' carbonate sands of Facies 2A (blue color)

Figure 6: Core from the area surrounding Bassas da India. A) Map showing locations of cores MOZ1-KS27 and MOZ4-CS22. B) Lithologic log, facies, event ages, and  $\delta^{18}\text{O}$  profile for core MOZ4-CS22. LR04 benthic stack for comparison. C) Representative carbonate and clastic facies from core MOZ4-CS22. For interval 1393-1443, X-radiograph reveals the presence of massive, unlaminated sediments at the bed base, and planar and ripple laminae in the upper part of the calciturbidite bed, forming a partial Bouma

(divisions A-C) sequence. D) Lithologic log, partial  $\delta^{18}\text{O}$  isotope profile, facies, and representative photos of carbonate-dominated beds in core MOZ1-KS27. Note mud clasts in right hand photo.

Figure 7: Grain size analysis of calcareous gravity flow beds. Y-axis = core depth in cm. Grey bars = percent grains (by volume) under  $63\ \mu\text{m}$  of sample size fraction 0-2mm (% mud). Yellow, red, and blue lines are D90, D50, and D10 grain size distributions, respectively. Interval generally captures allochthonous bed, though may also include some hemipelagic sedimentation atop and below bed, e.g., muddy samples at top and bottom of (E), where some coarser grains may be planktonic foraminifera tests. Facies denoted by colors corresponding to Figure 2. Chart (A) includes analysis of mud clasts within larger bed at 183 and 225 cm marks.

Figure 8: Compositional analysis of calcareous gravity flow beds. A) Examples of taxa seen in calciturbidite and calcidebrite beds, as observed in core MOZ4-CS09, in the interval between 338 and 340 cm. B) Coarse-grained (sand-sized and greater) component of selected of calciturbidite and calcidebrite beds in thin section. Samples shown here were washed and sieved ( $<63\ \mu\text{m}$  fraction removed). C) Composition of sediment samples taken at various depths within the same calciturbidite bed, showing progressive increase in foraminifera (blue). D) Composition of size-sieved sediment samples taken at the same depth within the same calciturbidite bed, showing increase in foraminifera content with smaller size fractions. E) Composition of various samples as determined by point counting. First 12 samples grouped into sea level phase (boundaries the same as shown in Figure 9B); latter three samples from with the MOZ1-KS27 calcidebrite bed for comparison. For C-E, the legend is shown above pie charts and raw count data can be found within the supplementary information section. Mud percentages also shown for most cores; the lower part of core MOZ4-CS22 was not able to be measured for logistical reasons.

Figure 9: Timing of gravity flow events in basins adjacent to Iles Eparses and relationships with global sea level. A) Data showing event age, sea level (from Spratt and Lisiecki, 2016), and the large-scale sea level trend at the time the event occurred. Events in orange were correlated between different cores and thus

only counted once; event beds in yellow text were excluded because of their clastic content, and event beds in blue were excluded due to their age. B) Compilation of ages of all recorded gravity flow events in last 800 ky, overlain on Lisieicki and Raymo sea level curve. Grey curves = 95% confidence interval; background color fields denote sea level phase referred to in (A). Time frame covered by cores shown to left (each core represented by one blue or pink vertical bars). C) Plot of gravity flow events vs absolute sea level (relative to present) at which they occurred. D) Histogram of event frequency in each phase of the sea level cycle. Value above each bar indicates the number of events per ky. E) Histogram of event frequency with respect to absolute sea level, relative to present. Sea level binned in 10-meter increments. Value next to each bar indicates the time sea level spent within a given 10-m depth range over the last 800 ky, calculated from the sea level curve of Spratt and Lisiecki (2016), as well as the actual number of events within that time frame.

Figure 10: General depositional model of carbonate gravity flow deposits seen in the Iles Eparses. Top diagram shows volcano-cored carbonate platform (left) and schematic basin-floor flow deposit. A-E represent idealized depositional profiles as discussed in the text.

Table 1: Collection parameters of core used in this study

Table 2: Definition of sea-level phases (highstand, transgression, regression, lowstand) used for compositional and event frequency analysis.

## REFERENCES

- Adams, A., & MacKenzie, I. (1998). Carbonate sediments and rocks under the microscope: a colour atlas. CRC Press, 184 p.
- Andresen, N., Reijmer, J. J., & Droxler, A. W. (2003). Timing and distribution of calciturbidites around a deeply submerged carbonate platform in a seismically active setting (Pedro Bank, Northern Nicaragua Rise, Caribbean Sea). *International Journal of Earth Sciences*, 92(4), 573-592.
- Bernet, K.H., Eberli, G.P. and Gilli, A., 2000, January. Turbidite frequency and composition in the distal part of the Bahamas transect. In *Proceedings of the Ocean Drilling Program, Scientific Results (Vol. 166, pp. 45-60)*. College Station, TX: Ocean Drilling Program.
- Betzler, C., Brachert, T. C., & Kroon, D. (1995). Role of climate in partial drowning of the Queensland Plateau carbonate platform (northeastern Australia). *Marine Geology*, 123(1-2), 11-32.
- Betzler, C., Fürstenau, J., Lüdman, T., Hübscher, C., Lindhorst, S., Paul, A., Reijmer, J., & Droxler, A. W. (2013) Sea-level and ocean-current control on carbonate-platform growth, Maldives, Indian Ocean. *Basin Research*, 25(2), 172-196.
- Bouma, A.H. (1962) *Sedimentology of some Flysch Deposits: A Graphic Approach to Facies Interpretation*. Elsevier, Amsterdam, 168 pp.
- Bourillet J., Ferry, J., Bourges P., 2013. PAMELA "Passive Margins Exploration Laboratories"; <https://doi.org/10.18142/236>
- Chabaud, L., Ducassou, E., Tournadour, E., Mulder, T., Reijmer, J.J., Conesa, G., Giraudeau, J., Hanquiez, V., Borgomano, J. and Ross, L., 2016. Sedimentary processes determining the modern carbonate periplatform drift of Little Bahama Bank. *Marine Geology*, 378, pp.213-229.

- Cochrane, D. J., Navarro, L., & Arnott, R. W. C. (2019) Sedimentological and geochemical evolution of an Ediacaran mixed carbonate-siliciclastic continental slope system, Windermere Supergroup, southern Canadian Cordillera, British Columbia, Canada. *Precambrian Research*, 327, 47-67.
- Cohen, K. M., Finney, S. C., Gibbard, P. L., & Fan, J. X. (2013) The ICS international chronostratigraphic chart. *Episodes*, 36(3), 199-204.
- Corlett, H. J., Bastesen, E., Gawthorpe, R. L., Hirani, J., Hodgetts, D., Hollis, C., & Rotevatn, A. (2018) Origin, dimensions, and distribution of remobilized carbonate deposits in a tectonically active zone, Eocene Thebes Formation, Sinai, Egypt. *Sedimentary Geology*, 372, 44-63.
- Counts, J. W., Jorry, S. J., Leroux, E., Miramontes, E., & Jouet, G. (2018) Sedimentation adjacent to atolls and volcano-cored carbonate platforms in the Mozambique Channel (SW Indian Ocean). *Marine Geology*, 404, 41-59.
- Counts, J. W., Jorry, S. J., Vazquez Riveiros, N., Jouet, G., Giraudeau, J., Chéron, S., Boissier, A., & Miramontes, E. (2019) A Late Quaternary record of highstand shedding from an isolated carbonate platform (Juan de Nova, southern Indian Ocean). *The Depositional Record*, 5, 540-557.
- Courgeon, S., Jorry, S. J., Camoin, G. F., BouDagher-Fadel, M. K., Jouet, G., Révillon, S., Bachèlery, P., Pelleter, E., Borgomano, J., Poli, E., & Droxler, A. W. (2016) Growth and demise of Cenozoic isolated carbonate platforms: New insights from the Mozambique Channel seamounts (SW Indian Ocean). *Marine Geology*, 380, 90-105.
- Courgeon, S., Jorry, S. J., Jouet, G., Camoin, G., BouDagher-Fadel, M. K., Bachèlery, P., Caline, B., Révillon, S., Thomas, Y., Thereau, E., & Guerin, C. (2017). Impact of tectonic and volcanism on the Neogene evolution of isolated carbonate platforms (SW Indian Ocean). *Sedimentary Geology*, 355, 114-131.

- Crevello, P. D., & Schlager, W. (1980) Carbonate debris sheets and turbidites, Exuma Sound, Bahamas. *Journal of Sedimentary Research*, 50(4), 1121-1147.
- Da Silva, A. C., Potma, K., Weissenberger, J. A., Whalen, M. T., Humblet, M., Mabilie, C., & Boulvain, F. (2009) Magnetic susceptibility evolution and sedimentary environments on carbonate platform sediments and atolls, comparison of the Frasnian from Belgium and Alberta, Canada. *Sedimentary Geology*, 214(1-4), 3-18.
- Deville, E., Marsset, T., Courgeon, S., Jatiault, R., Ponte, J.P., Thereau, E., Jouet, G., Jorry, S.J., Droz, L. (2018) Active fault system across the oceanic lithosphere of the Mozambique Channel: Implications for the Nubia–Somalia southern plate boundary. *Earth Planet. Sci. Lett.* 502, 210–220.
- Droxler, A.W. and Schlager, W., 1985. Glacial versus interglacial sedimentation rates and turbidite frequency in the Bahamas. *Geology*, 13(11), pp.799-802.
- Droxler, A. W., Haddad, G. A., Mucciarone, D. A., & Cullen, J. L. (1990) 29. Pliocene-Pleistocene aragonite cyclic variations in holes 714a and 716b (the Maldives) compared with hole 633a (the Bahamas): Records of climate-induced CaCO<sub>3</sub> preservation at intermediate water depths. In: Duncan, R.A., Backman, J., Peterson, L.C., et al., (eds.) *Proceedings of the Ocean Drilling Program, Scientific Results*. 115, 539-577.
- Drzewiecki, P. A., & Simó, J. A. (2002) Depositional processes, triggering mechanisms and sediment composition of carbonate gravity flow deposits: examples from the Late Cretaceous of the south-central Pyrenees, Spain. *Sedimentary Geology*, 146(1-2), 155-189.
- Dunham, R. J., 1962, Classification of carbonate Rocks according to depositional texture. In: Ham, W. E. (ed.), *Classification of carbonate Rocks: American Association of Petroleum Geologists Memoir*, p. 108-121.
- Everts, A. J. (1991) Interpreting compositional variations of calciturbidites in relation to platform-stratigraphy: an example from the Paleogene of SE Spain. *Sedimentary Geology*, 71(3-4), 231-242.

- Fierens, R., Toucanne, S., Droz, L., Jouet, G., Raisson, F., Jorissen, E.L., Bayon, G., Giraudeau, J. & Jorry, S.J., 2020. Quaternary sediment dispersal in the Zambezi turbidite system (SW Indian Ocean). *Marine Geology* 428.
- Gledhill, D.K., Wanninkhof, R., Millero, F.J., Eakin, C.M., 2008. Ocean acidification of the Greater Caribbean Region 1996–2006. *J. Geophys. Res.* 113, C10031.
- Haak, A. B., & Schlager, W. (1989) Compositional variations in calciturbidites due to sea-level fluctuations, late Quaternary, Bahamas. *Geologische Rundschau*, 78(2), 477-486.
- Haflidason, H., Lien, R., Sejrup, H. P., Forsberg, C. F., & Bryn, P. (2005) The dating and morphometry of the Storegga Slide. In: Solheim, A., Bryn, P., Berg, K., Sejrup, H.P., and Mienert, J. (eds.): *Ormen Lange—An Integrated Study for Safe Field Development in the Storegga Submarine Area*. Elsevier. 123-136.
- Haughton, P. D., Barker, S. P., & McCaffrey, W. D. (2003) ‘Linked’debrites in sand-rich turbidite systems—origin and significance. *Sedimentology*, 50(3), 459-482.
- Haughton, P., Davis, C., McCaffrey, W., & Barker, S. (2009) Hybrid sediment gravity flow deposits—classification, origin and significance. *Marine and Petroleum Geology*, 26(10), 1900-1918.
- International Seismological Centre (2019), On-line Bulletin, <https://doi.org/10.31905/D808B830>
- Johns, D. R., Mutti, E., Rosell, J., & Seguret, M. (1981) Origin of a thick, redeposited carbonate bed in Eocene turbidites of the Hecho Group, south-central Pyrenees, Spain. *Geology*, 9(4), 161-164.
- Jorry S. J. (2014) PTOLEMEE cruise, L’Atalante R/V. <https://doi.org/10.17600/14000900>
- Jorry, S.J., Droxler, A.W., Francis, J.M. (2010) Deepwater carbonate deposition in response to re-flooding of carbonate bank and atoll-tops at glacial terminations. *Quat. Sci. Rev.* 29, 2010–2026

Jorry, S.J., Camoin, G.F., Jouet, G., Le Roy, P., Vella, C., Courgeon, S., Prat, S., Fontanier, C., Paumard, V., Boule, J., Caline, B., Borgomano, J. (2016) Modern sediments and Pleistocene reefs from isolated carbonate platforms (Iles Eparses, SW Indian Ocean): A preliminary study. *Acta Oecologica-Int. J. Ecol.* 72, 129–143.

Jorry, S.J., Jouet, G., Edinger, E. N., Toucanne, S., Counts, J. W., Miramontes, E., Courgeon, S., Vazquez-Riveiros, N., Le Roy, P., & Camoin, G. F. (2020) From platform top to adjacent deep sea: New source-to-sink insights into carbonate sediment production and transfer in the SW Indian Ocean (Glorieuses archipelago). *Marine Geology*, 423, 106-144.

Jorry, S. J., Droxler, A. W., Mallarino, G., Dickens, G. R., Bentley, S. J., Beaufort, L., Bentley, S. J., Beaufort, L., Peterson, L.C., & Opdyke, B. N. (2008) Bundled turbidite deposition in the central Pandora Trough (Gulf of Papua) since Last Glacial Maximum: Linking sediment nature and accumulation to sea level fluctuations at millennial timescale. *Journal of Geophysical Research: Earth Surface*, 113(F1S19), 1-15.

Jouet G., Deville E. (2015) PAMELA-MOZ04 cruise, RV Pourquoi pas?. <https://doi.org/10.17600/15000700>

Kalvoda, J., Bábek, O., & Malovaná, A. (1999) Sedimentary and biofacies records in calciturbidites at the Devonian-Carboniferous boundary in Moravia (Moravian-Silesian Zone, Middle Europe). *Facies*, 41(1), 141-157.

Kenter, J. A. (1990) Carbonate platform flanks: slope angle and sediment fabric. *Sedimentology*, 37(5), 777-794.

Lantsch, H., Roth, S., Reijmer, J. J., & Kinkel, H. (2007) Sea-level related resedimentation processes on the northern slope of Little Bahama Bank (Middle Pleistocene to Holocene). *Sedimentology*, 54(6), 1307-1322.

Lee, K., Tong, L.T., Millero, F.J., Sabine, C.L., Dickson, A.G., Goyet, C., Park, G.H., Wanninkhof, R., Feely, R.A., & Key, R.M. (2006) Global relationships of total alkalinity with salinity and temperature in surface waters of the world's oceans. *Geophys. Res. Lett.* 33, L19605.

Leroux, E., Counts, J. Jorry S., Jouet G., Révillon S., BouDagher-Fadel, M.K., Courgeon, S., Berthod, C., Ruffet, G., Bachèlery, P., & Grenard-Grand E. (2020) Evolution of the Glorieuses seamount in the SW Indian Ocean and surrounding deep Somali Basin since the Cretaceous. *Marine Geology*, in press.

Lisiecki, L.E., & Raymo, M.E. (2005) A Pliocene-Pleistocene stack of 57 globally distributed benthic  $\delta^{18}\text{O}$  records. *Paleoceanography*, 20(1).

Lowe, D.R., 1982. Sediment gravity flows II. Depositional models with special reference to the deposits of high-density turbidity currents. *J. Sediment. Petrol.* 52, 279–297.

Maurer, F., Reijmer, J. J. G., & Schlager, W. (2003) Quantification of input and compositional variations of calciturbidites in a Middle Triassic basinal succession (Seceda, Dolomites, Southern Alps). *International Journal of Earth Sciences*, 92(4), 593-609.

Mazzullo, S. J., & Mazzullo, L. J. (1983). Atoll Reservoir Facies in Pennsylvanian Limestone Higgins Ranch Field, Coke County, Texas.

Miller, K. G., Mountain, G. S., Wright, J. D., & Browning, J. V. (2011) A 180-million-year record of sea level and ice volume variations from continental margin and deep-sea isotopic records. *Oceanography*, 24(2), 40-53.

Milliman, J. D., Müller, G., & Förstner, F. (1974). Recent sedimentary carbonates: Part 1 marine carbonates. Springer Science & Business Media.

Miramontes, E., Jorry, S.J., Jouet, G., Counts, J.W., Courgeon, S. Le Roy, P. Guerin, C. and Hernández-Molina, F. J. (2019) Deep-water dunes on drowned isolated carbonate terraces (Mozambique Channel, south-west Indian Ocean). *Sedimentology* 66(4), 1222-1242.

Mulder, T., & Alexander, J. (2001) The physical character of subaqueous sedimentary density flows and their deposits. *Sedimentology*, 48(2), 269-299.

Olu, K., (2014) PAMELA-MOZ01 cruise, L'Atalante R/V. <https://doi.org/10.17600/14001000>

Paillard, D., Labeyrie, L. D., & Yiou, P. (1996) AnalySeries 1.0: a Macintosh software for the analysis of geophysical time-series. *Eos*, 77, 379.

Paul, A., Reijmer, J. J., Fürstenau, J., Kinkel, H., & Betzler, C. (2012) Relationship between Late Pleistocene sea-level variations, carbonate platform morphology and aragonite production (Maldives, Indian Ocean). *Sedimentology*, 59(5), 1640-1658.

Payros, A., & Pujalte, V. (2008) Calciclastic submarine fans: An integrated overview. *Earth-Science Reviews*, 86(1-4), 203-246.

Prat, S., Jorry, S. J., Jouet, G., Camoin, G., Vella, C., Le Roy, P., Caline, B., Boichard, R., & Pastol, Y. (2016) Geomorphology and sedimentology of a modern isolated carbonate platform: The Glorieuses archipelago, SW Indian Ocean. *Marine Geology*, 380, 272-283.

Peyrotty, G., Rigaud, S., Kemkin, I., & Martini, R. (2020) Sedimentology and biostratigraphy of upper Triassic atoll-type carbonates from the Dalnegorsk area, Taukha terrane, far East Russia. *Global and Planetary Change*, 184, 103072.

Puga-Bernabéu, Á., Webster, J.M., Beaman, R.J., Guilbaud, V., 2013. Variation in canyon morphology on the Great Barrier Reef margin, north-eastern Australia: the influence of slope and barrier reefs.

*Geomorphology* 191, 35–50.

Puga-Bernabéu, Á., Webster, J.M., Beaman, R.J., 2014, Reimer, P., Renema, W., 2014. Filling the gap: a 60 ky record of mixed carbonate-siliciclastic turbidite deposition from the Great Barrier Reef. *Marine and Petroleum Geology* 50, 40–50.

Reijmer, J. J. G., Schlager, W., Bosscher, H., Beets, C. J., & McNeill, D. F. (1992) Pliocene/Pleistocene platform facies transition recorded in calciturbidites (Exuma Sound, Bahamas). *Sedimentary Geology*, 78(3-4), 171-179.

Reijmer, J. J. G., Sprenger, A., Ten Kate, W. G. H. Z., Schlager, W., & Krystyn, L. (1994) Periodicities in the composition of Late Triassic calciturbidites (eastern Alps, Austria). *Orbital forcing and cyclic sequences*, 19, 323-343.

Reijmer, J. J., Palmieri, P., & Groen, R. (2012) Compositional variations in calciturbidites and calcidebrites in response to sea-level fluctuations (Exuma Sound, Bahamas). *Facies*, 58(4), 493-507.

Reijmer, J. J., Palmieri, P., Groen, R., & Floquet, M. (2015) Calciturbidites and calcidebrites: Sea-level variations or tectonic processes?. *Sedimentary Geology*, 317, 53-70.

Robertson, A. H. F. (1976) Pelagic chalks and calciturbidites from the lower Tertiary of the Troodos Massif, Cyprus. *Journal of Sedimentary Research*, 46(4), 1007-1016.

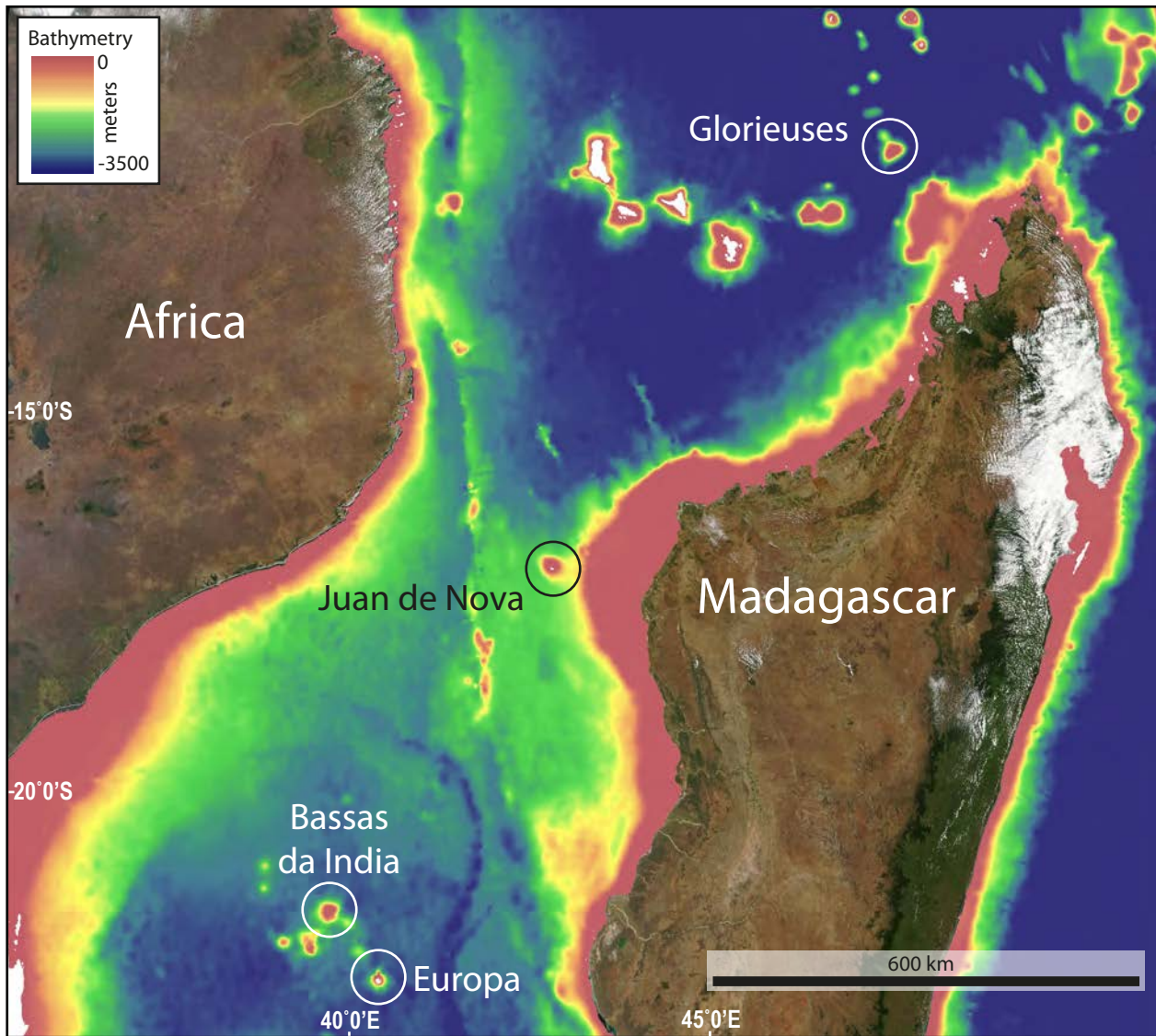
Roduit, N. (2019) JMicroVision: Image analysis toolbox for measuring and quantifying components of high-definition images. Version 1.3.1. <https://jmicrovision.github.io> (accessed 5 August 2020)

Rubert, Y., Jati, M., Loisy, C., Cerepi, A., Foto, G., & Muska, K. (2012) Sedimentology of resedimented carbonates: Facies and geometrical characterisation of an upper Cretaceous calciturbidite system in Albania. *Sedimentary Geology*, 257, 63-77.

Schlager, W., Reijmer, J. J., & Droxler, A. (1994) Highstand shedding of carbonate platforms. *Journal of Sedimentary Research*, 64(3b), 270-281.

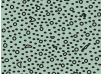
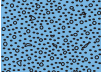
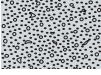
- Shanmugam, G. (2016) Submarine fans: a critical retrospective (1950–2015). *Journal of Palaeogeography*, 5(2), 110-184.
- Sola, F., Puga-Bernabéu, Á., Aguirre, J., Braga, J.C., 2018. Origin, evolution and sedimentary processes associated with a late Miocene submarine landslide, southeast Spain. *Sedimentary Geology*, 364, 351–366.
- Spence, G. H., & Tucker, M. E. (1997) Genesis of limestone megabreccias and their significance in carbonate sequence stratigraphic models: a review. *Sedimentary Geology*, 112(3-4), 163-193.
- Spratt, R. M., & Lisiecki, L. E. (2016). A late Pleistocene sea level stack. *Climate of the Past*, 12, 1079–1092. <https://doi.org/10.5194/cp-12-1079-2016>
- Sudiro, P. (2002) Carbonate slope deposits of the Contrin formation, Costabella area (Western dolomites, NE Italy). *Mem. della Soc. Geol. Ital*, 57(1), 19-28.
- Thiéblemont, A., Hernandez-Molina, F. J., Ponte, J. P., Robin, C., Guillocheau, F., Cazzola, C., & Raison, F. (2020) Seismic stratigraphic framework and depositional history for Cretaceous and Cenozoic contourite depositional systems of the Mozambique Channel, SW Indian Ocean. *Marine Geology*, 425, 106-192.
- Webster, J.M., Beaman, R.J., Puga-Bernabéu, Á., Ludman, D., Renema, W., Wust, R.A.J., George, N.P.J., Reimer, P.J., Jacobsen, G.E., 2012. Late Pleistocene history of turbidite sedimentation in a submarine canyon off the northern Great Barrier Reef, Australia. *Palaeogeogr. Palaeoclimatol. Palaeoecol.* 331-332, 75-89.
- Winefield, P., Burgess, P., Minzoni, M., Pierson, B., Playton, T., & Janson, X. (2011) Deep-Water Resedimented Carbonate Exploration Play Types: Controls and Models. *AAPG Search and Discovery Article 50502*.

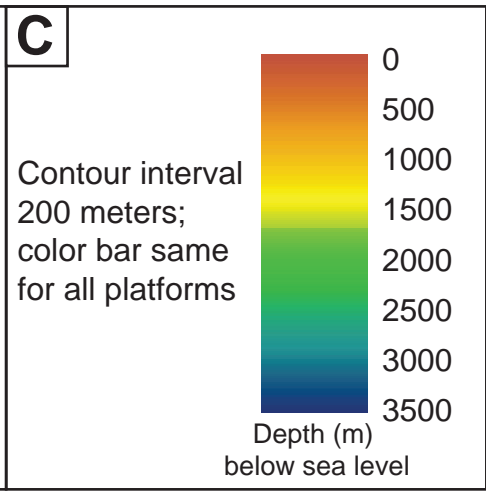
Xu, J., Wang, P., Huang, B., Li, Q., & Jian, Z. (2005) Response of planktonic foraminifera to glacial cycles: Mid-Pleistocene change in the southern South China Sea. *Marine Micropaleontology*, 54(1-2), 89-105.

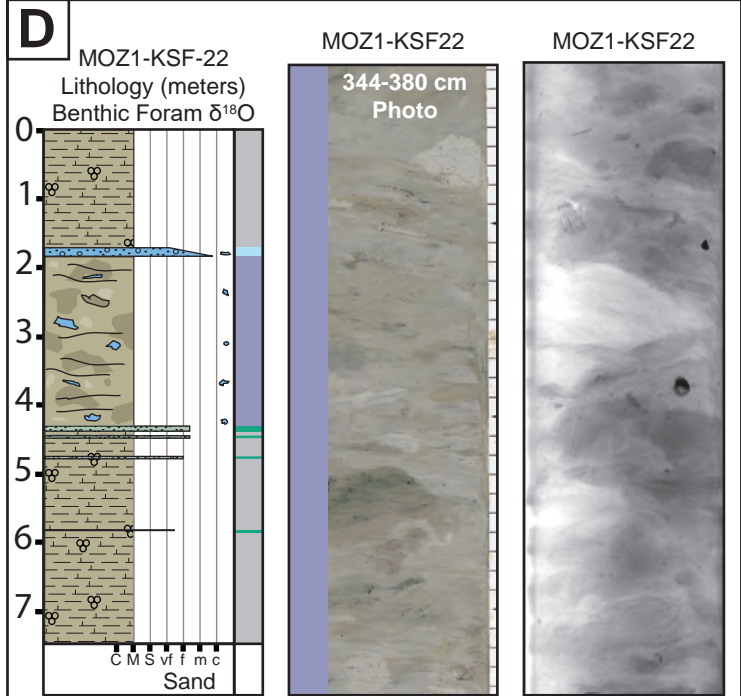
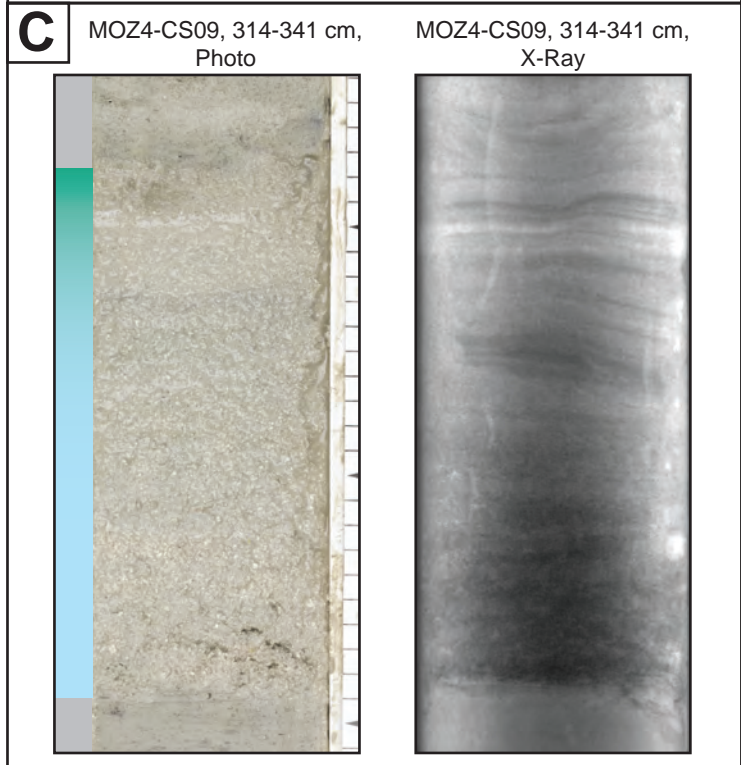
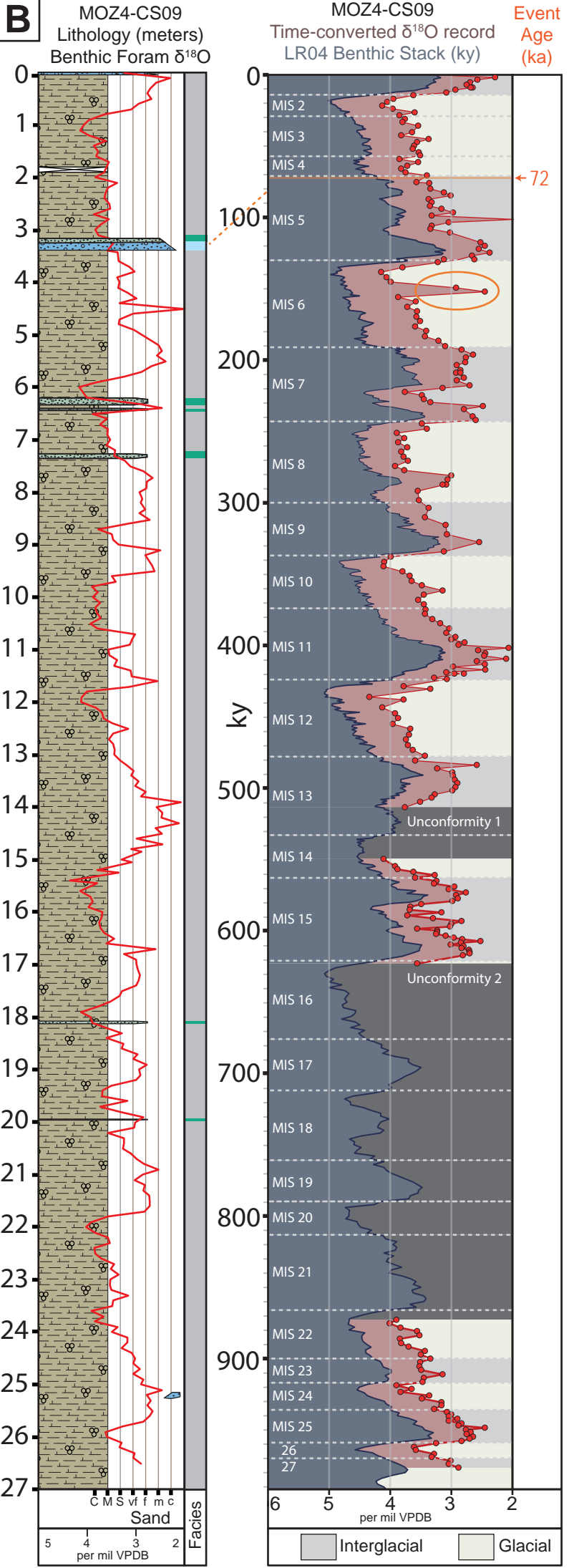
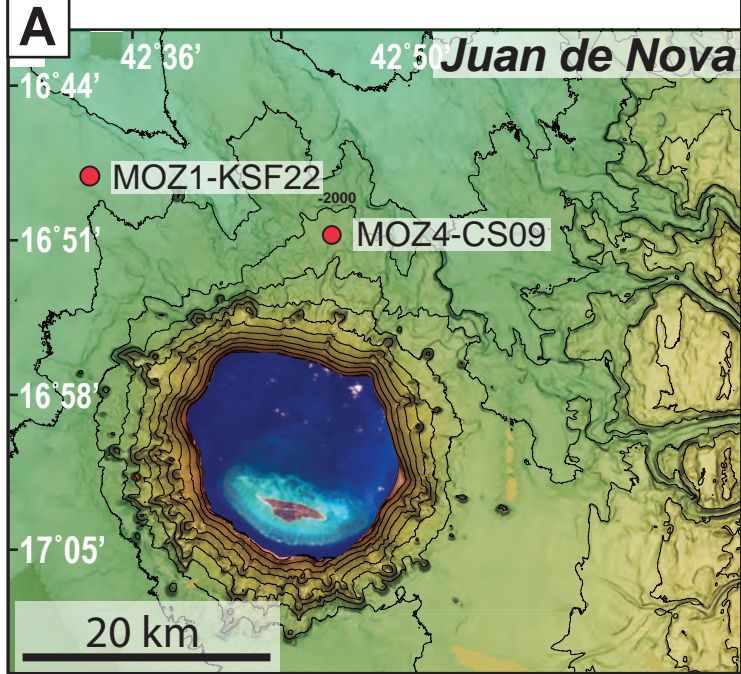


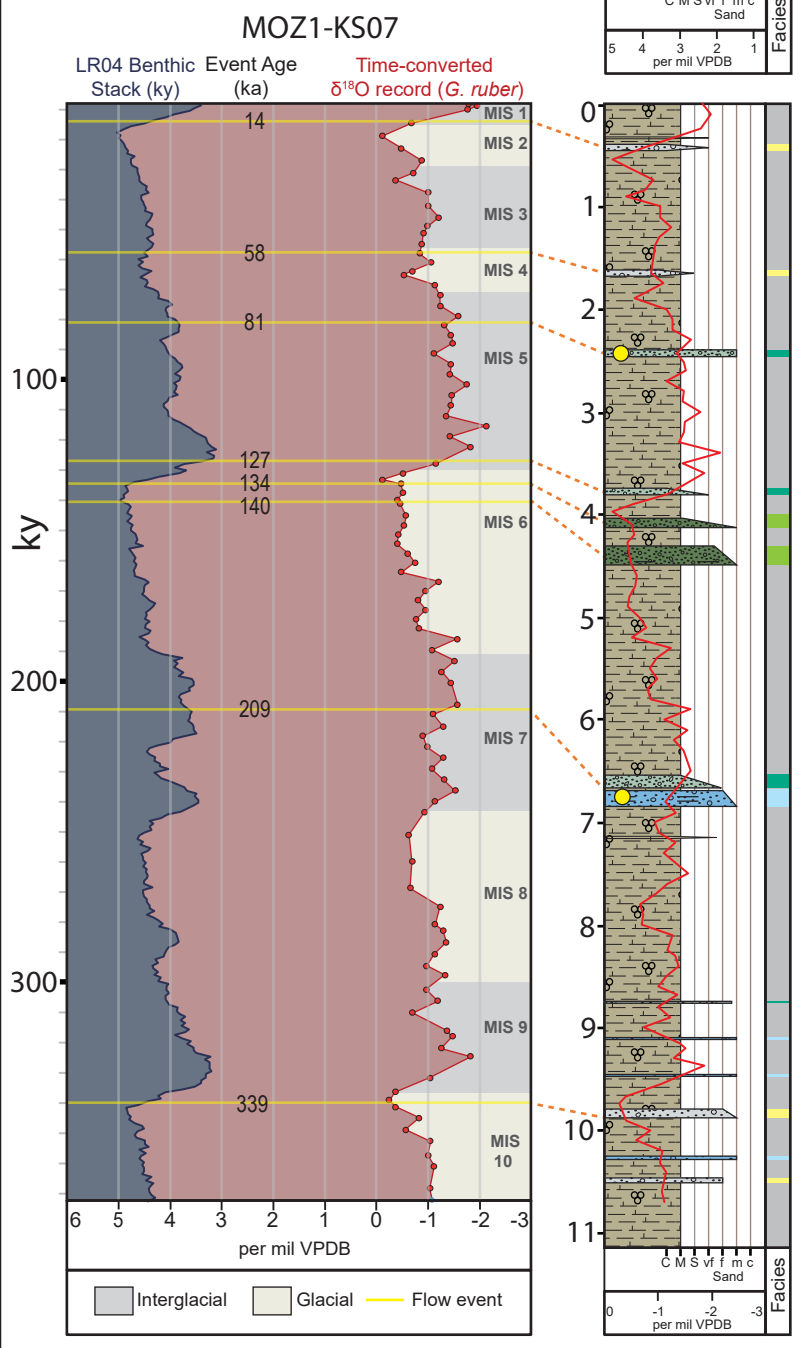
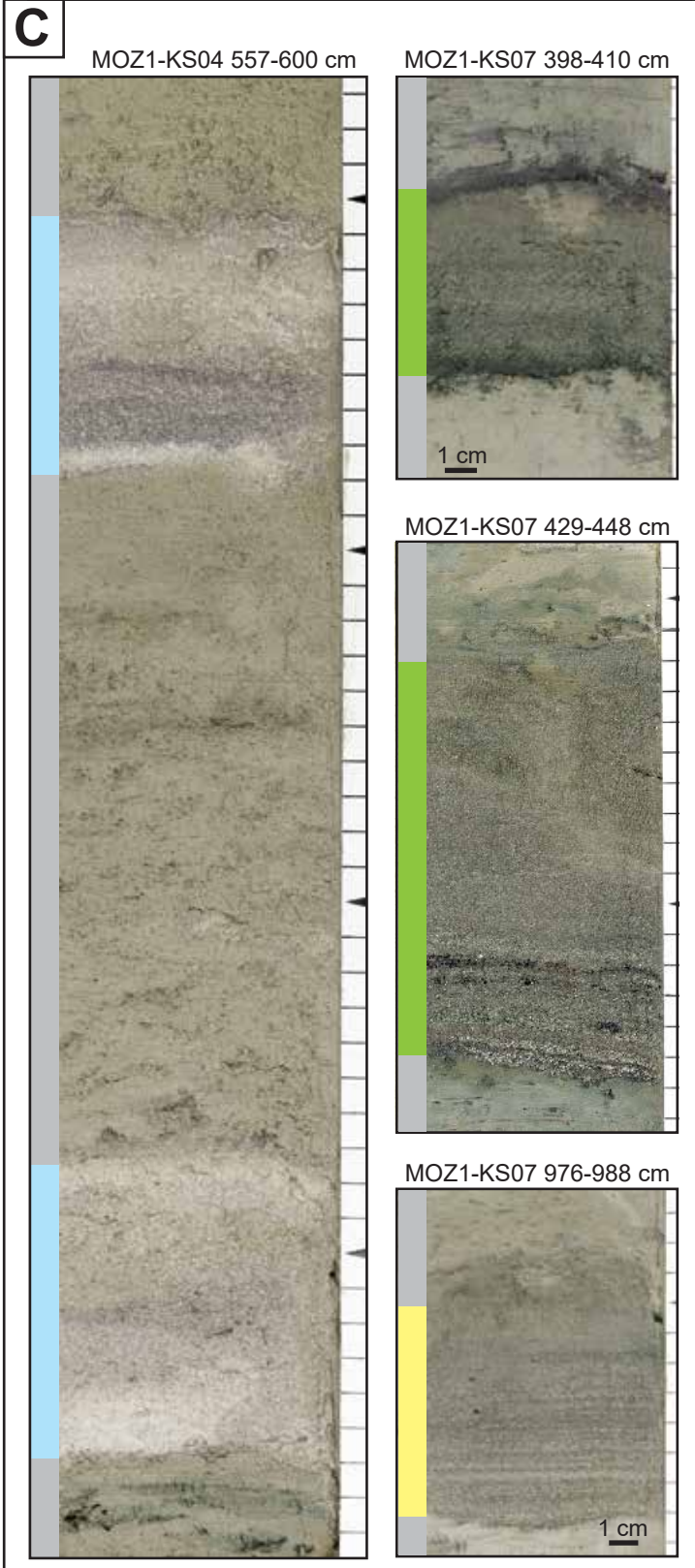
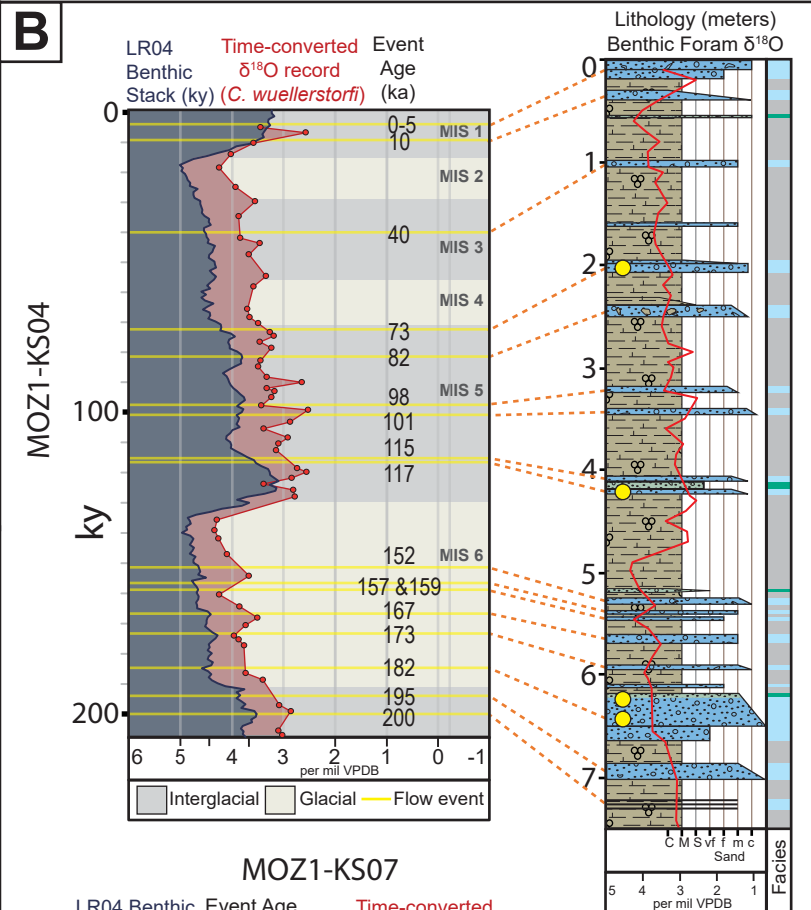
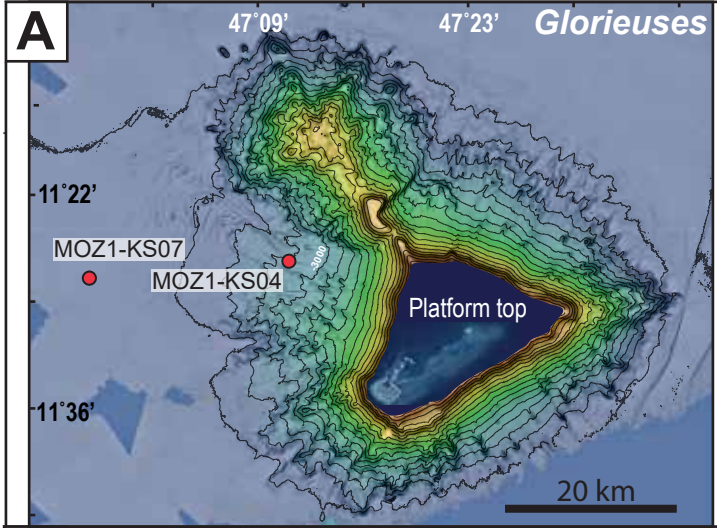
<b>A</b>	Facies 1	Laminated or bioturbated hemipelagic and aragonitic muds with foraminifera tests
	Facies 2	Chaotically bedded, clast-bearing muds
	Facies 3	Massive, fining-, or coarsening-upward carbonate packstones
	Facies 4	Massive, fining-, or coarsening-upward carbonate wackestones
	Facies 5	Carbonate packstones containing cm-scale mudclasts
	Facies 6	Clastic sandy muds or muddy sands
	Facies 7	Mixed lithology sands containing glauconite, clastic, and carbonate grains

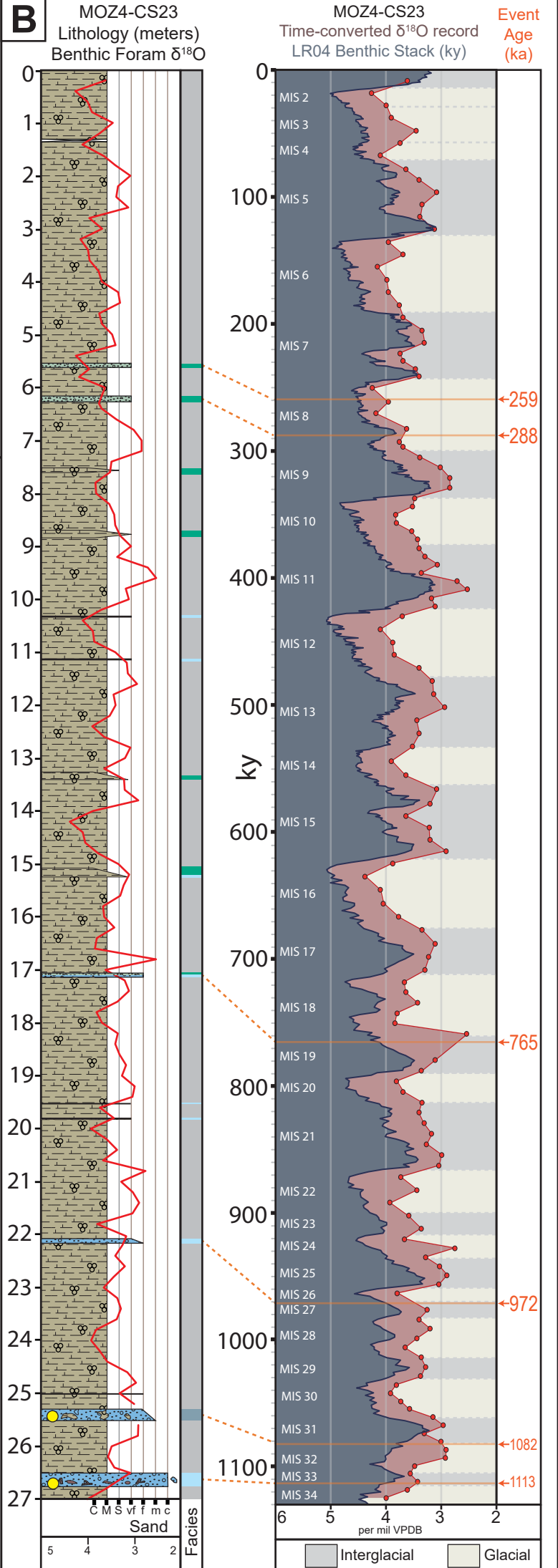
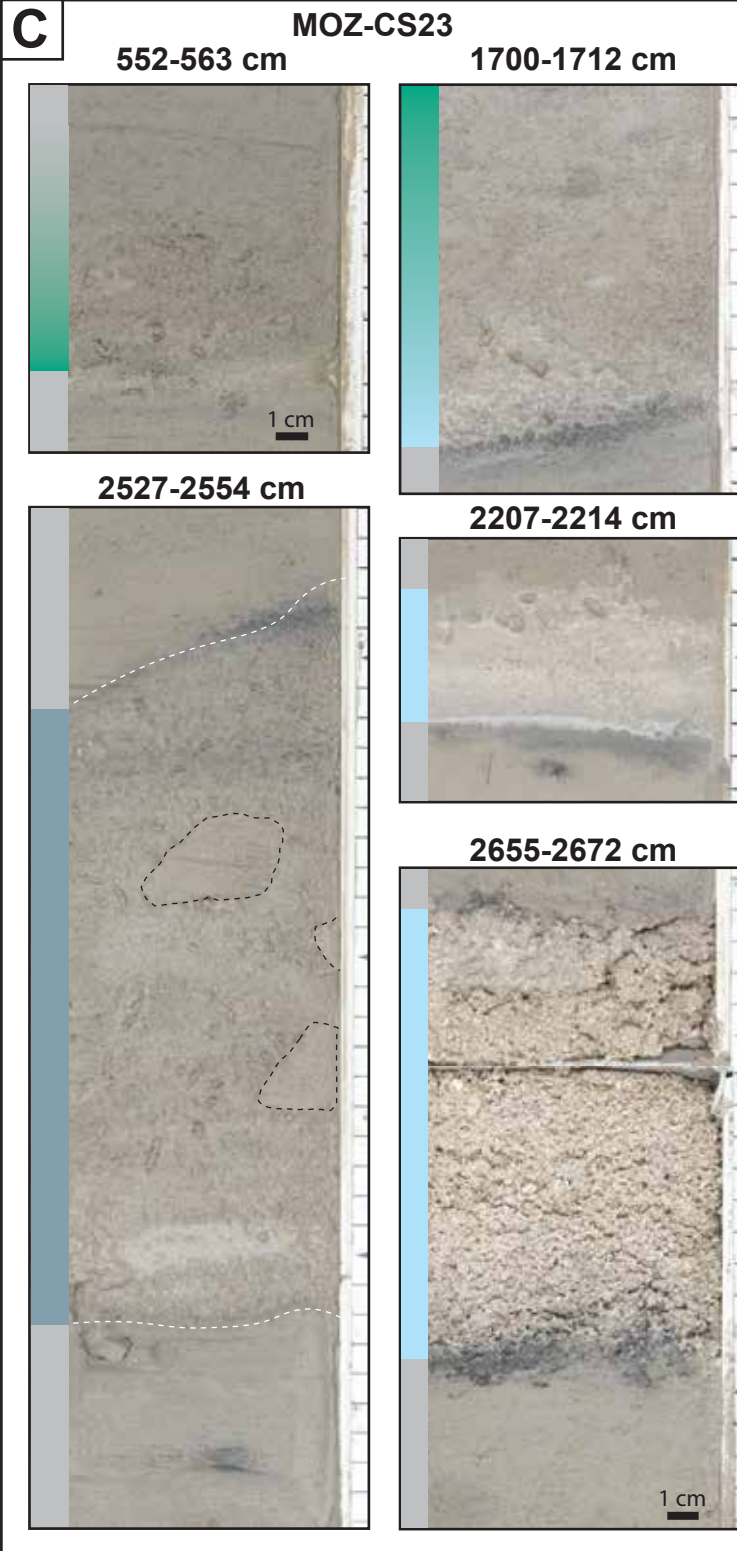
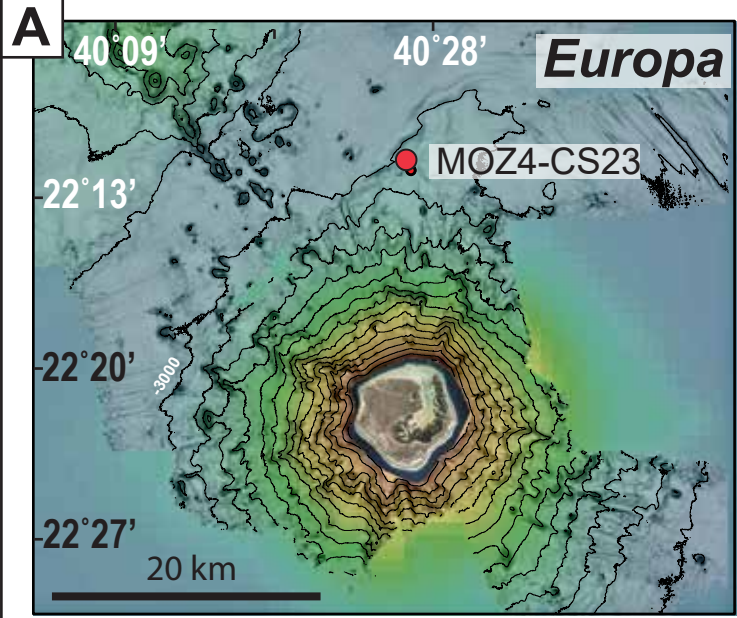
**B**

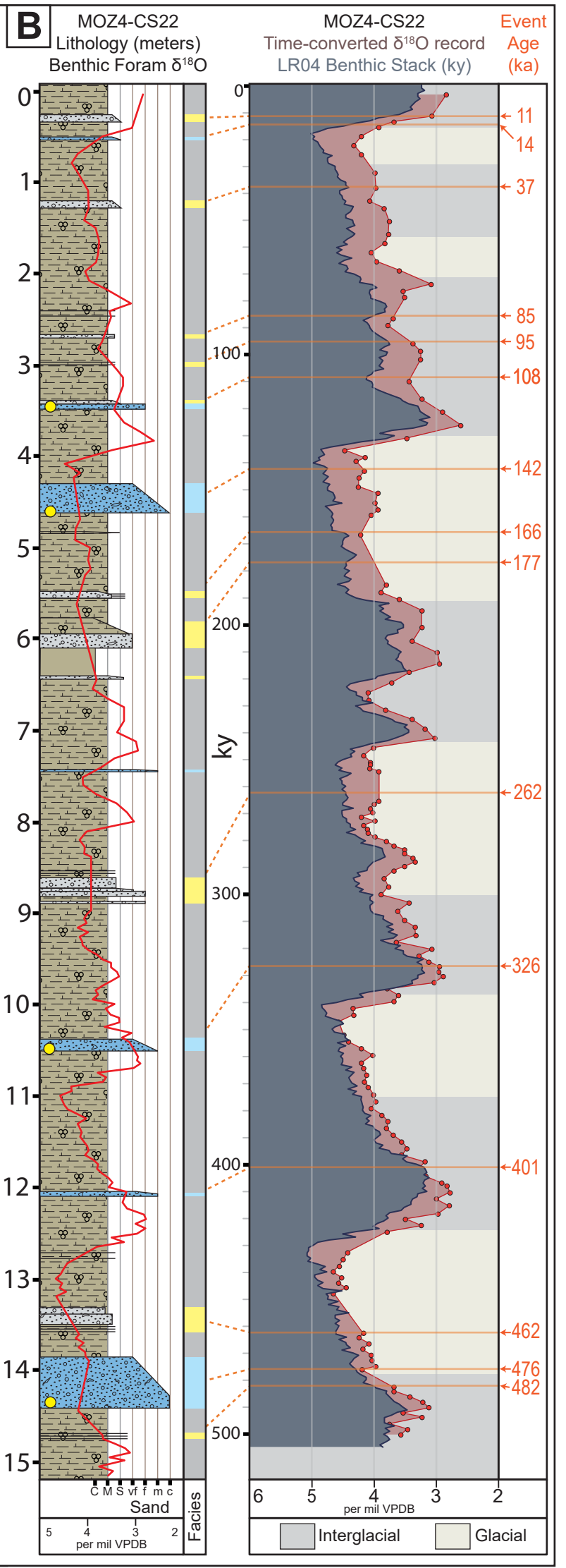
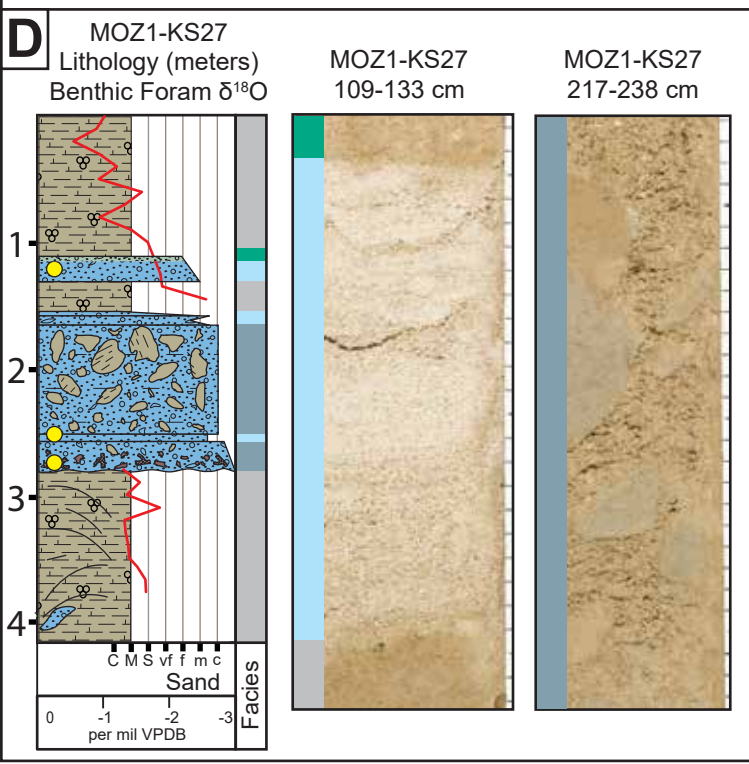
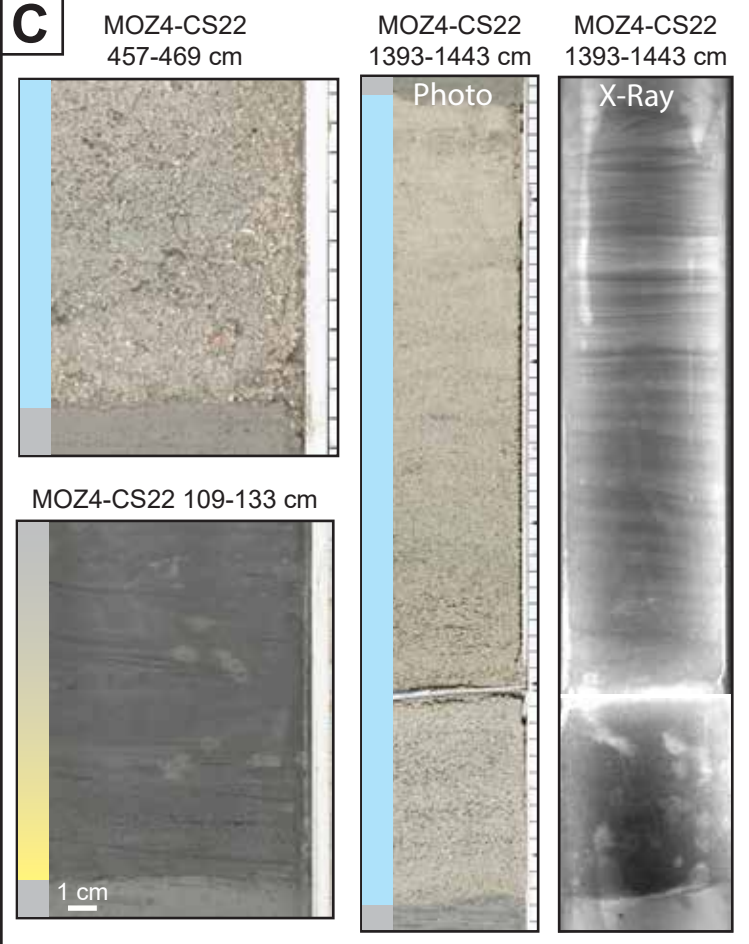
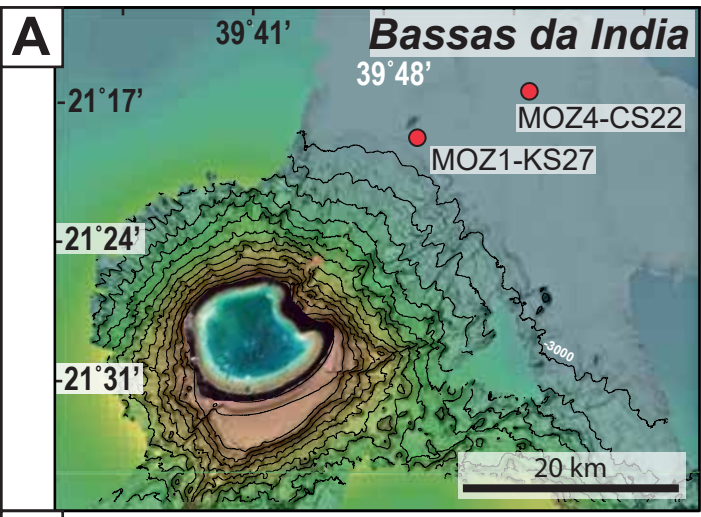
	Foram. mud		Chaotically organized muds
	Carbonate Wackestone		Mud clasts
	Carbonate Packstone		Skeletal fragments
	Glauconitic Sand		Carbonate clasts
	Clastic Sand		Deformed laminae

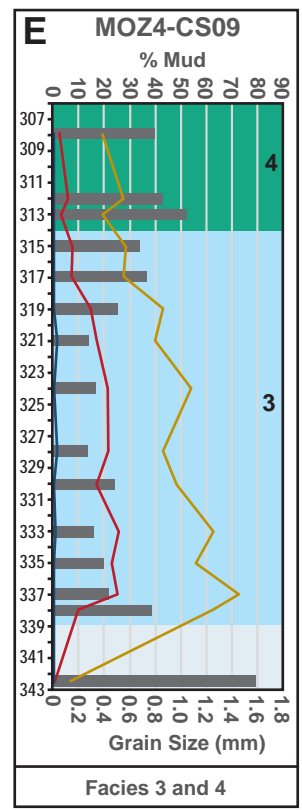
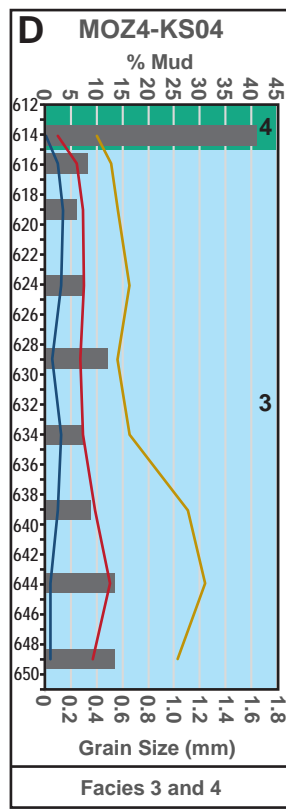
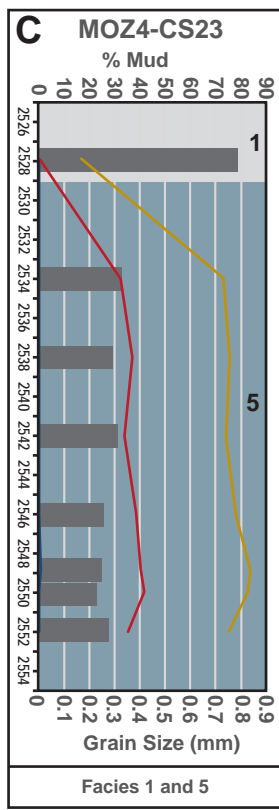
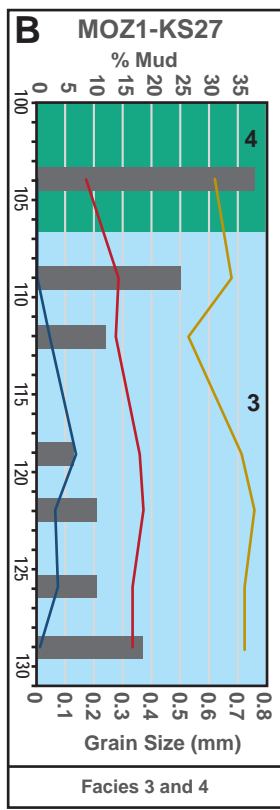
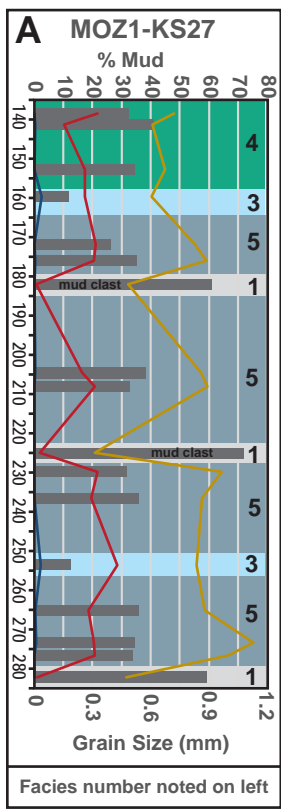








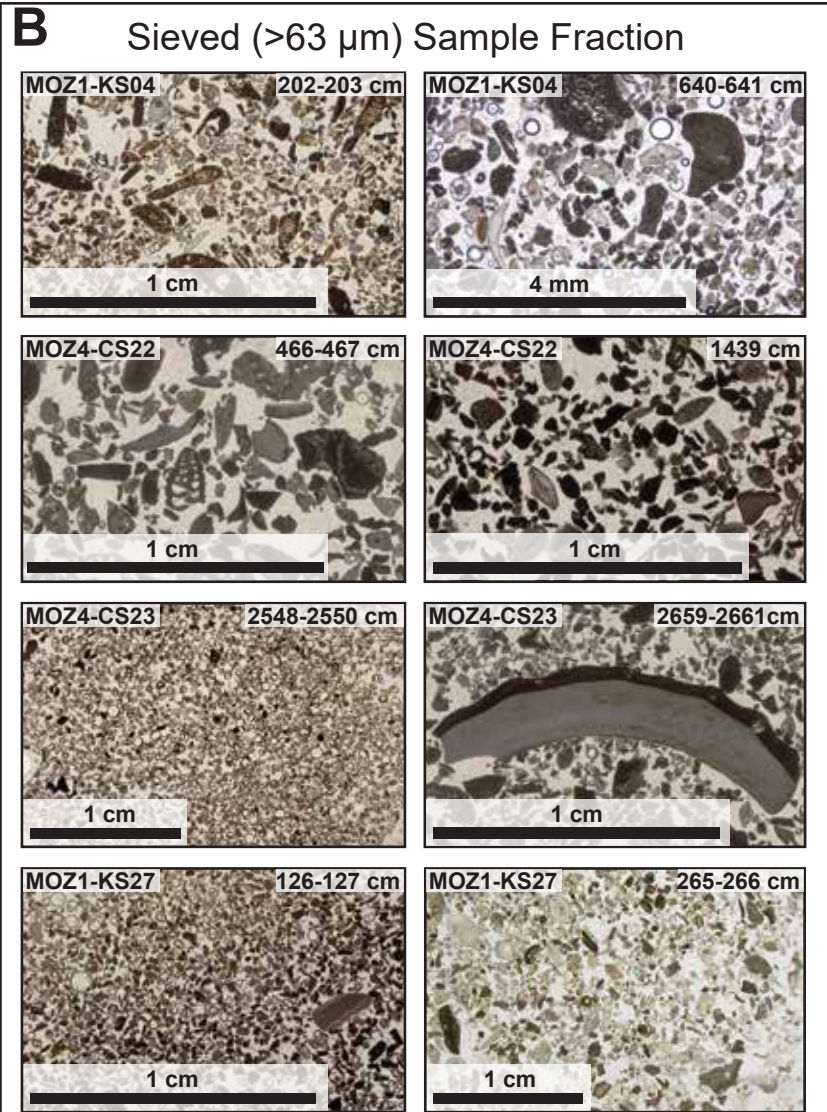
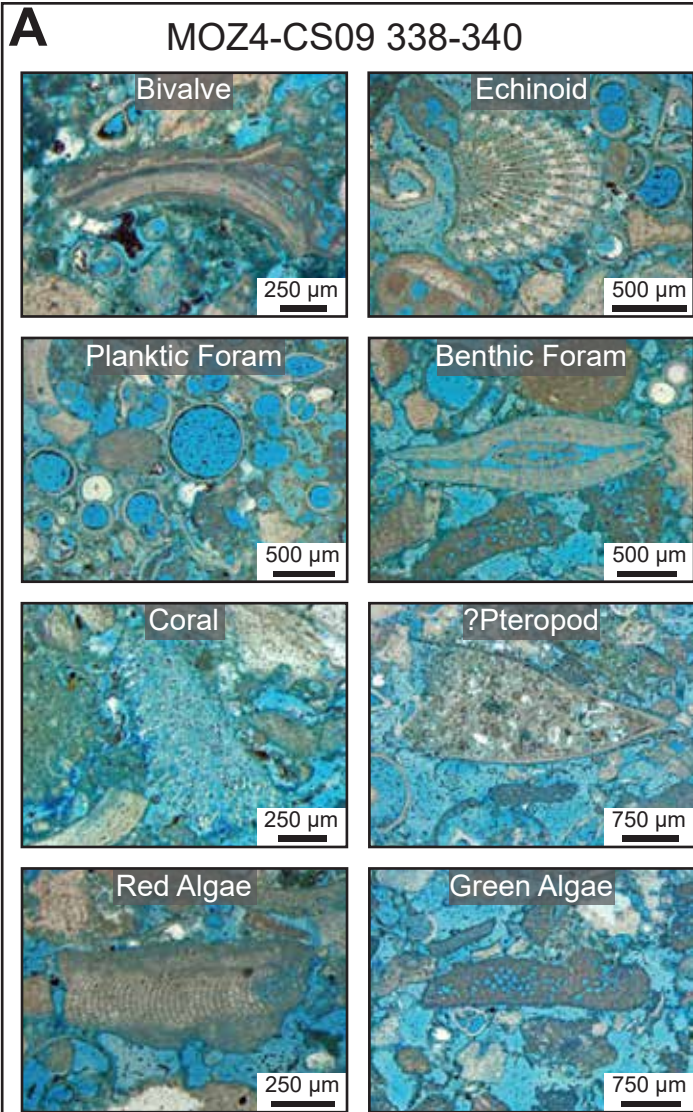




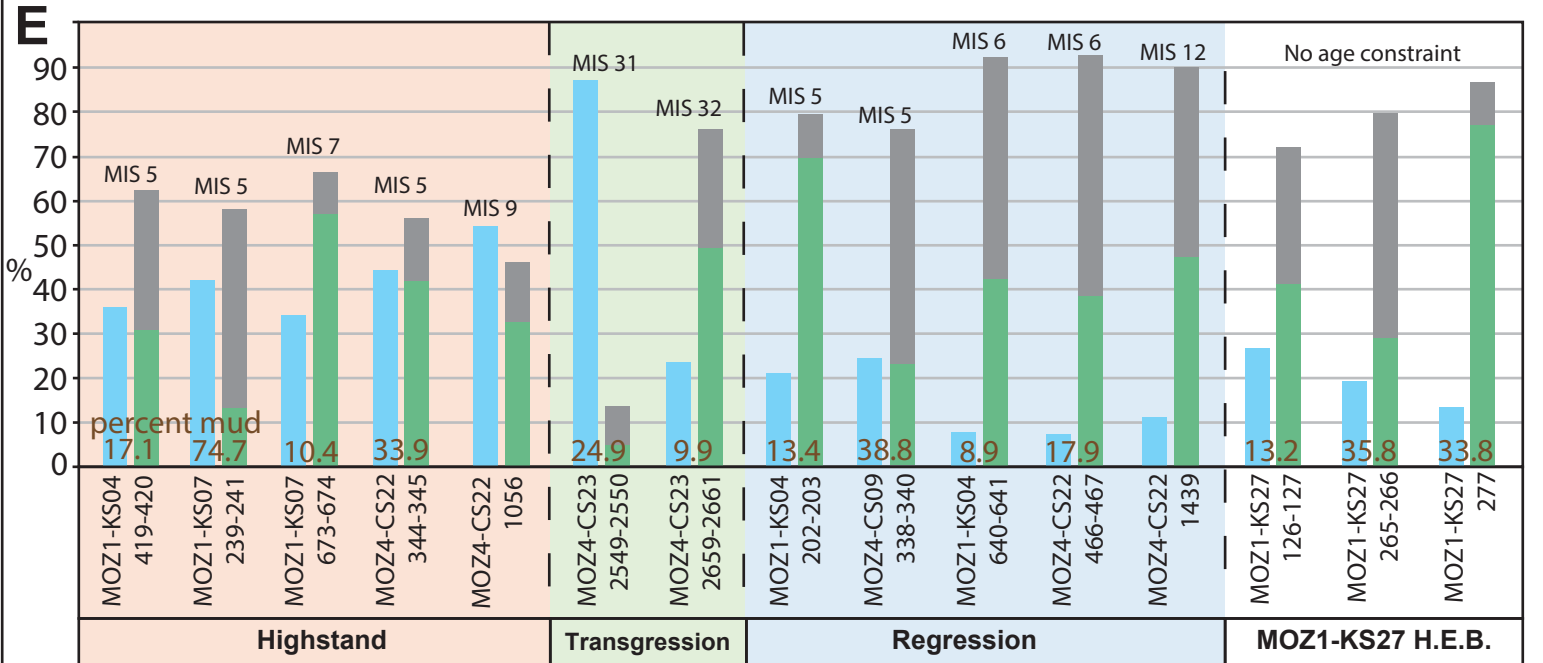
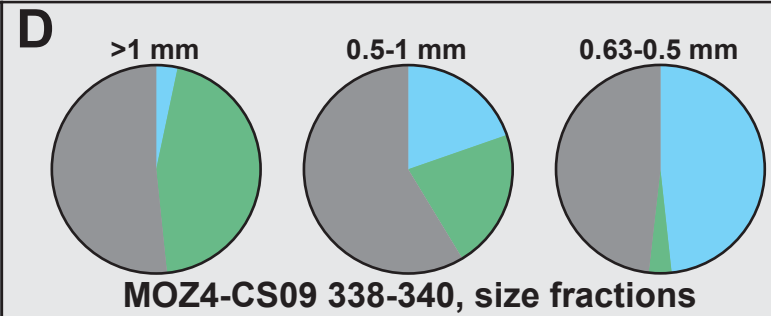
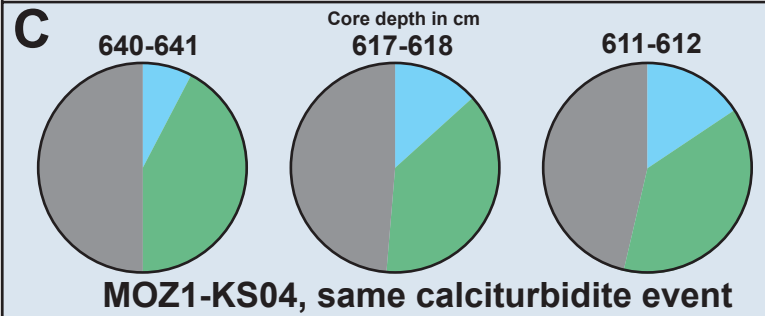
Y Axes = Core depth in cm

Grey bars = Percent mud (<63 μm)

Grain size distributions — D90 — D50 — D10



Compositional Trends Foraminifera Calcareous Algae Skeletal Frag. / Unidentified



MOZ1-KS04		
Event Age	SL	SL Trend
2.5 (avg)	4.75	Trans.
10	-23.18	Trans.
40	-83.13	Regress.
73	-38.44	Regress.
82	-31.47	HS
98	-19.34	HS
101	-16.69	HS
115	-29.37	HS
117	-17.04	HS
152	-80.76	Regress.
157	-87.48	Regress.
159	-86.43	Regress.
167	-60.97	Regress.
173	-59.51	Regress.
182	-61.87	Regress.
195	-27.93	Regress.
200	-10.01	HS

Orange = Correlated Event

MOZ1-KS07		
Event Age	SL	SL Trend
14	-75.97	Trans.
58	-81.85	Regress.
81	-32.68	HS
127	-26.94	Trans.
134	-119.82	Trans.
140	-120.22	Regress.
209	-9.22	HS
339	-89.68	Trans.

Yellow = Clastic Bed

MOZ4-CS09		
Event Age	SL	SL Trend
72	-43.6	Regress.

MOZ4-CS23		
Event Age	SL	SL Trend
259	-86.91	LS
288	-54.86	Trans.
765	-39.26	Regress.
972	-50	Regress.
1082	-38.6667	Trans.
1113	-50	Trans.

\* from Miller et al., 2011

MOZ4-CS22		
Event Age	SL	SL Trend
11	-36.19	Trans.
14	-75.97	Trans.
37	-93.4	Regress.
85	-29.96	HS
95	-34.94	HS
108	-42.91	HS
142	-110.49	Regress.
166	-64.42	Regress.
177	-57.08	Regress.
262	-72.1	LS
326	-11.59	HS
401	17.75	HS
462	-78.29	Regress.
476	-29.84	Regress.
482	-30.53	Regress.

Yellow = Clastic Bed

